

Novel WRN Helicase Inhibitors Selectively Target Microsatellite-Unstable Cancer Cells



Gabriele Picco¹, Yanhua Rao², Angham Al Saedi¹, Yang Lee², Sara F. Vieira¹, Shriram Bhosle¹, Kieron May⁶, Carmen Herranz-Ors¹, Samantha J. Walker¹, Raynold Shenje², Cansu Dincer¹, Freddy Gibson¹, Ruby Banerjee¹, Zoe Hewitson¹, Thilo Werner⁴, Joshua E. Cottom², Yang Peng², Nanhua Deng⁵, Youyou Zhang², Eldridge N. Nartey², Leng Nickels², Philip Landis², Daniela Conticelli⁷, Katrina McCarten¹, Jacob Bush³, Mamta Sharma¹, Howard Lightfoot¹, David House³, Emma Milford³, Emma K. Grant³, Michal P. Glogowski², Craig D. Wagner², Marcus Bantscheff⁴, Anna Rutkowska-Klute⁴, Cell Model Network UK Group, Francesca Zappacosta², Jonathan Pettinger³, Syd Barthorpe¹, H. Christian Eberl⁴, Brian T. Jones⁸, Jessica L. Schneck², Dennis J. Murphy², Emile E. Voest⁹, Joshua P. Taygerly⁸, Michael P. DeMartino², Matthew A. Coelho¹, Jonathan Houseley⁶, Geeta Sharma⁵, Benjamin Schwartz⁵, and Mathew J. Garnett¹

ABSTRACT

Microsatellite-unstable (MSI) cancers require WRN helicase to resolve replication stress due to expanded DNA (TA)_n dinucleotide repeats. WRN is a promising synthetic lethal target for MSI tumors, and WRN inhibitors are in development. In this study, we used CRISPR-Cas9 base editing to map WRN residues critical for MSI cells, validating the helicase domain as the primary drug target. Fragment-based screening led to the development of potent and highly selective WRN helicase covalent inhibitors. These compounds selectively suppressed MSI model growth *in vitro* and *in vivo* by mimicking WRN loss, inducing DNA double-strand breaks at expanded TA repeats and DNA damage. Assessment of biomarkers in preclinical models linked TA-repeat expansions and mismatch repair alterations to compound activity. Efficacy was confirmed in immunotherapy-resistant organoids and patient-derived xenograft models. The discovery of potent, selective covalent WRN inhibitors provides proof of concept for synthetic lethal targeting of WRN in MSI cancer and tools to dissect WRN biology.

SIGNIFICANCE: We report the discovery and characterization of potent, selective WRN helicase inhibitors for MSI cancer treatment, with biomarker analysis and evaluation of efficacy *in vivo* and in immunotherapy-refractory preclinical models. These findings pave the way to translate WRN inhibition into MSI cancer therapies and provide tools to investigate WRN biology.

See related commentary by Wainberg, p. 1369

INTRODUCTION

Microsatellite instability (MSI) characterizes mismatch repair (MMR)-deficient cancers and is prevalent in colorectal, endometrial, and gastric tumors, among others (1, 2). Some arise from somatic MMR defects, others more rarely from germline mutations, such as those in Lynch syndrome—a genetic condition associated with MMR gene mutations. MSI tumors typically are associated with better prognosis, fewer metastases, and increased survival (3, 4), likely due to distinct pathologic and molecular characteristics. The profusion of neoantigens generated by their hypermutated profile predisposes them to immunologic interventions, especially when immune checkpoints are blocked (5), a process mediated by both adaptive and innate immune responses (6). This underpins the transformative impact of immune checkpoint inhibitors (ICI) on the clinical management of MSI tumors, further advanced by neoadjuvant ICI treatments (7–9). Some MSI tumors are aggressive, and innate and acquired resistance to ICI is common, especially in the metastatic setting (10–12), underscoring the need for new therapeutic strategies.

WRN helicase is involved in maintaining genome integrity, and germline mutations cause Werner syndrome, which is characterized by premature ageing and increased cancer risk

(13, 14). Recent work uncovered a synthetic lethal relationship between loss of the WRN RecQ-like helicase and MSI cancers (15–18). Mechanistic dissection traced WRN dependency to the accumulation of expanded DNA TA dinucleotide repeats in MSI cells, which formed cytotoxic DNA secondary structures requiring WRN for resolution (19).

A genetic dependency on WRN is observed in a diverse set of MSI colorectal cancer preclinical models, including those resistant to standard-of-care treatments (20). This discovery has prompted efforts to target WRN pharmacologically as a novel precision strategy against MSI tumors, alone or in combination with other therapies. Small-molecule WRN inhibitors (WRNi) were developed before the discovery of the WRN-MSI synthetic lethal interaction (18, 21) but have limited potency and selectivity (22, 23). Recently, a new WRNi was reported (24), and two more (25–27) have entered clinical trials (NCT05838768 and RO7589831), but a detailed description of their activity, particularly in preclinical models, has not been reported and prevents an assessment of their therapeutic potential. Thus, developing potent and selective WRN helicase inhibitors and their detailed preclinical evaluation remains an important next step to validate the synthetic-lethal effect of WRN in MSI tumors following pharmacologic inhibition.

Here, we report the discovery of novel potent, selective covalent inhibitors which bind the WRN helicase domain and provide a comprehensive evaluation of their activity in preclinical models and potential biomarkers to refine patient stratification. These inhibitors mimic genetic WRN loss, induce DNA damage, and selectively suppress MSI cancer cell model growth, including in patient-derived organoids, tumor xenografts, and patient-derived xenograft (PDX) models of immunotherapy-resistant disease. Our findings serve as proof of concept for pharmacologic targeting WRN's helicase activity, paving the way for precision therapies for MSI tumors and enhancing our understanding of WRN biology.

¹Wellcome Sanger Institute, Cambridge, UK. ²GSK, Upper Providence, Pennsylvania. ³GSK, Stevenage, UK. ⁴GSK Heidelberg, Germany. ⁵GSK, Cambridge, Massachusetts. ⁶Epigenetics Programme, Babraham Institute, Cambridge, UK. ⁷Candiolo Cancer Institute, Turin, Italy. ⁸IDEAYA Biosciences, South San Francisco, California. ⁹Netherlands Cancer Institute, Amsterdam, the Netherlands.

Corresponding Authors: Gabriele Picco, Wellcome Sanger Institute, Cambridge CB10 1SA, UK. E-mail: gabriele.picco@sanger.ac.uk; and Mathew J. Garnett, mathew.garnett@sanger.ac.uk

Cancer Discov 2024;14:1457–75

doi: 10.1158/2159-8290.CD-24-0052

©2024 American Association for Cancer Research

RESULTS

Mapping of Targetable Domains in WRN Using Semisaturating Mutagenesis

WRN has helicase and exonuclease enzymatic activity and germline loss of function variants associated with Werner syndrome are distributed across the gene footprint. Thus, to investigate the role of specific WRN domains in the synthetic lethal interaction with MSI, we used CRISPR base editing to introduce single-nucleotide WRN variants in two MSI cancer cell lines and assessed effects on growth. We engineered colorectal KM12 and endometrial RL95-2 cells to express adenine base editor (ABE) and cytosine base editor (CBE) doxycycline-inducible NGN base editors with high activity (Supplementary Fig. S1A and S1B; refs. 28, 29). Base editor cell lines were transduced with a 3735-guide library (Fig. 1A) comprising guides targeting WRN exons/promoters ($n = 3,107$) and controls including nontargeting ($n = 57$), intergenic ($n = 168$), and stop codon-introducing single-guide RNAs (sgRNA) for essential ($n = 307$) and nonessential ($n = 87$) genes (Supplementary Table S1). This mutagenesis aimed to modify >70% of WRN amino acids via CBE and ABE (Supplementary Fig. S1C). However, given variable sgRNAs' efficiency, nonsignificant scores do not definitively exclude a residue's functional importance.

To evaluate WRN variant effects, we introduced the sgRNA library into MSI cells, induced base editor expression, and cultured cells for 10 days before quantifying sgRNAs via next-generation sequencing (Supplementary Fig. S1D; Supplementary Table S2). We observed depletion of essential gene-targeting sgRNAs, validating known essential genes and reproducibility (Supplementary Fig. S2A and S2B). Combining ABE and CBE screen results showed that most sgRNAs targeting introns or predicted to cause synonymous mutations had neutral effects. In contrast, those likely causing missense mutations or splice variants were preferentially depleted (Supplementary Fig. S2C).

Our strategy identified residues required for WRN-MSI synthetic lethality, providing a map of critical WRN protein domains. We examined sgRNAs targeting the WRN coding sequence (Fig. 1B) and aligned our findings with AlphaMissense predictions (30). Regions predicted pathogenic by AlphaMissense showed an increased number of hits, thus supporting our screening approach (Fig. 1B and C). Although the exonuclease catalytic activity was considered nonessential for WRN-MSI synthetic lethality (15, 16), some sgRNAs in this domain scored as hits. However, many of these edits install prolines, potentially causing protein misfolding (31). Essential residues were identified in the WRNIP1 interaction motif, which overlaps with the exonuclease domain (Supplementary Fig. S2D). The lack of vulnerability in WRNIP1-knockout MSI cells (15, 32) suggests the WRNIP1 motif of WRN might have additional functions. Crucially, the helicase domain showed hit enrichment (Fig. 1B; Supplementary Fig. S2E), particularly in the ATP-binding subdomain, with specific residues having remarkable intolerance to variation. The comparative analysis of our screen results across both models demonstrated a uniform sgRNA depletion pattern (Fig. 1D; $R^2 = 0.77$ for CBE, 0.69 for ABE), confirming the essential role of these amino acids in MSI cell viability, regardless of the model or tissue. Finally, we mapped critical sites for targeting

WRN-MSI synthetic lethality on the crystal structure of the WRN helicase domain (33), highlighting residues intolerant to variation and their proximity to the catalytic center (Fig. 1E).

Overall, base editing maps of amino acid essentiality provide insights into WRN functionality, reinforcing the pivotal role of the ATP-binding helicase domain in WRN-MSI lethality, with the potential to inform the structure-guided design of WRNis.

Reactive Fragment-Based Screening Identifies Potent and Selective Covalent Small-Molecule WRN Helicase Inhibitors

Base editing screens successfully pinpointed critical residues on WRN essential for its synthetic lethality in MSI cancer cells. Building on these findings, we aimed to develop inhibitors for the WRN helicase through a fragment-based screening approach (Fig. 2A; ref. 34). Using intact-protein LC/MS, we screened a library of methyl acrylate-based reactive fragments against the WRN helicase domain and identified a promising hit compound, GSK_WRN1, which gave rapid single covalent modification of WRN, achieving 81% labeling efficiency at 20 $\mu\text{mol/L}$ concentration within 24 hours at 21 °C (Supplementary Fig. S3A). Tryptic digest of the WRN-GSK_WRN1 adduct and LC/MS-MS analysis revealed that the covalent hit was selectively modifying Cys727 (Supplementary Fig. S3B). A focused medicinal chemistry effort was initiated to enhance biochemical potency and cellular selectivity for *in vivo* use, details of which will be presented in a subsequent report. This resulted in several compounds progressively developed from the same chemical series, including GSK_WRN2, GSK_WRN3, and GSK_WRN4 (Fig. 2B). Preliminary biochemical characterization showed that GSK_WRN3 and GSK_WRN4 significantly improved upon the inhibitory potency against WRN helicase activity compared to earlier compounds, with pIC_{50} values of 8.6 and 7.6 respectively, underscoring their enhanced efficacy over GSK_WRN1 (5.8) and GSK_WRN2 (6.5; Supplementary Fig. S3C).

We investigated the selectivity of this compound series. Using a fluorescence-based assay to evaluate ATPase activity (35), GSK_WRN4 had exceptional specificity for WRN over other RecQ helicases (Fig. 2C). Next, we employed a mass spectrometry (MS)-based quantitative chemoproteomic workflow (36) for cysteine-ome profiling of GSK_WRN4 in Jurkat cells. Remarkably, of 23,602 distinct cysteine-containing peptides across the proteome, WRN Cys727 was the only observed site that was almost completely modified (Fig. 2D). Even at 50 $\mu\text{mol/L}$ GSK_WRN4, few further cysteines were significantly modified demonstrating the remarkable specificity of the compound (Supplementary Fig. S3D). Introducing knock-in mutations at Cys727 rendered colorectal cancer MSI SW48 isogenic models resistant to WRN inhibition, despite having a neutral effect in the absence of the drug (Fig. 2E; Supplementary Fig. S3E).

Notably, WRN Cys727 is unique to WRN among helicase family members (Supplementary Fig. S3F), likely underscoring the selectivity observed over the other RecQ helicases.

To assess the molecular phenotype induced by these compounds, we performed a proteomics analysis using one of our early lead compounds GSK_WRN2. Treatment of the MSI cell

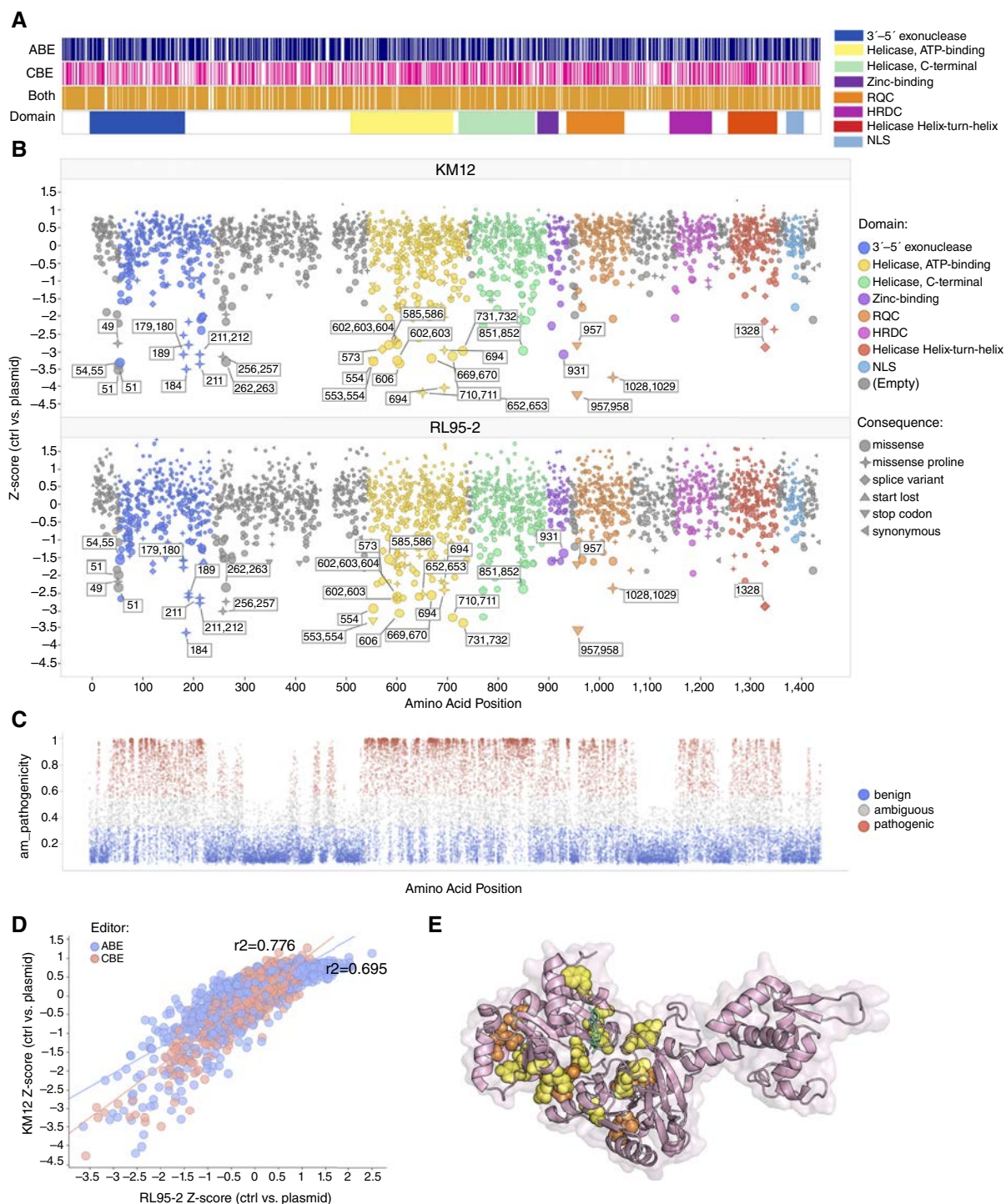


Figure 1. Functional interrogation of WRN domains using base editing screens in MSI cells. **A**, Heatmap of predicted cytosine and adenine base editing sites across WRN amino acids. Individual and combined putative edits are overlaid with the main WRN protein domains. **B**, Functional variant mapping of WRN for KM12 (top) and RL95-2 (bottom). Z-scores from the base editing screens for each sgRNA are displayed across WRN protein domains. sgRNAs that are referenced in the text and that introduce potential Loss of Function (LOF) and Gain of Function (GOF) positions are highlighted with their predicted edited amino acid locations. Screen z-scores for each base editor were determined individually and are shown side by side for comparison. The size of each dot in the graph is proportional to the value of the Z-score. **C**, Missense variants are represented as dots, plotted based on their AlphaMissense (AM) pathogenicity scores (y-axis) vs. their amino acid positions (x-axis of **B**). Variants predicted to be pathogenic (red), likely benign variants (blue), and ambiguous ones (gray) were highlighted as downloaded from the AlphaMissense database (30). **D**, Correlation between KM12 (y-axis) and RL95-2 (x-axis) z-scores, with ABE screens in red and CBE screens in blue. **E**, The crystal structure of the WRN helicase domain (PDB ID: 6YHR) highlighting residues intolerant to variation identified by base editing screens. Missense edits predicted to introduce proline are marked in orange, whereas other missense variants are indicated in yellow. ATP analogue AMP-PNP in green has been mapped onto the WRN structure. (Figure components were created with BioRender.com).

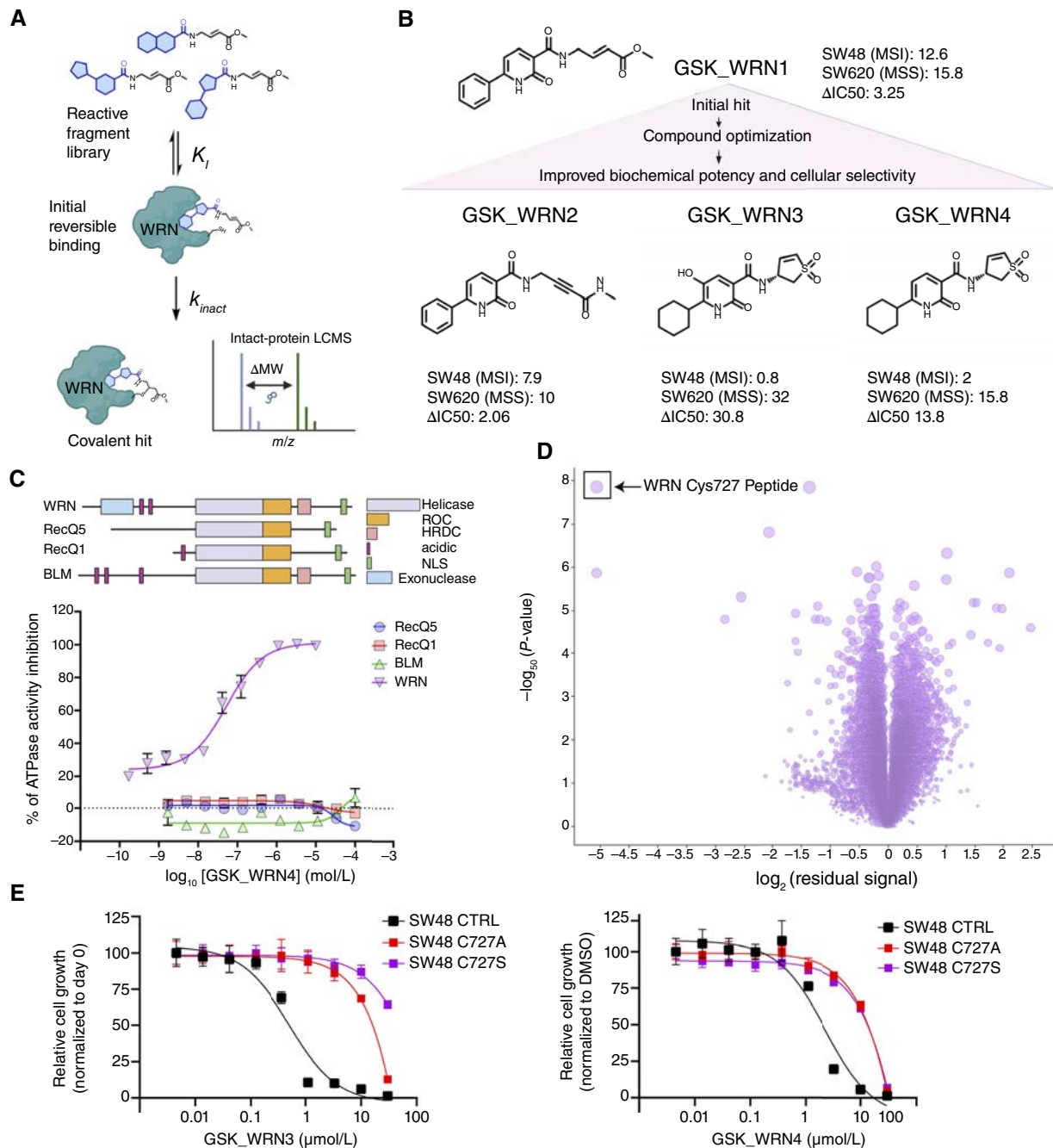


Figure 2. Fragment-based screening identifies potent and selective small-molecule WRN helicase inhibitors. **A**, Schematic overview of the fragment-based screening strategy used. **B**, Structures of the WRN helicase compounds identified, from the initial hit fragment to the optimized compounds. The IC_{50} s ($\mu\text{mol/L}$) are reported for MSI and MSS cell lines. **C**, Selectivity analysis shows GSK_WRN4 exhibits specificity toward WRN compared with other RecQ family helicases. The schematics above represent the main functional domains of RecQ DNA helicases BioRender.com. **D**, Volcano plot of quantitative reactive cysteine profiling of Jurkat cells treated with 10 $\mu\text{mol/L}$ GSK_WRN4. The GSK_WRN4 target cysteine residue WRN Cys727 is indicated. **E**, The relative growth of SW48 control and isogenic cells (C727A and C727S) when treated with GSK_WRN3 (left) and GSK_WRN4 (right) inhibitors. Growth is normalized to DMSO controls and plotted against inhibitor concentrations. Data points reflect average values, with error bars showing the SD of three technical replicates. (C, Created with BioRender.com.)

line SW48 with 10 $\mu\text{mol/L}$ GSK_WRN2 for 48 hours led to a significant reduction in WRN protein ($\log_2FC = -7.1$, adjusted P value = 3.1×10^{-6} ; Supplementary Fig. S3G), consistent with reports of WRNis leading to chromatin-associated degradation (bioRxiv 2023.12.08.570895). Additionally, GSK_WRN2

induced CDKN1A (p21) and ALDH3A1, markers indicative of DNA damage and oxidative stress, respectively. Gene set enrichment analysis (GSEA) highlighted a reduction in genes crucial for cell-cycle progression (*CCNB1*, *NUSAP1*, and *KIF2C*), chromosome dynamics (chromatid separation and

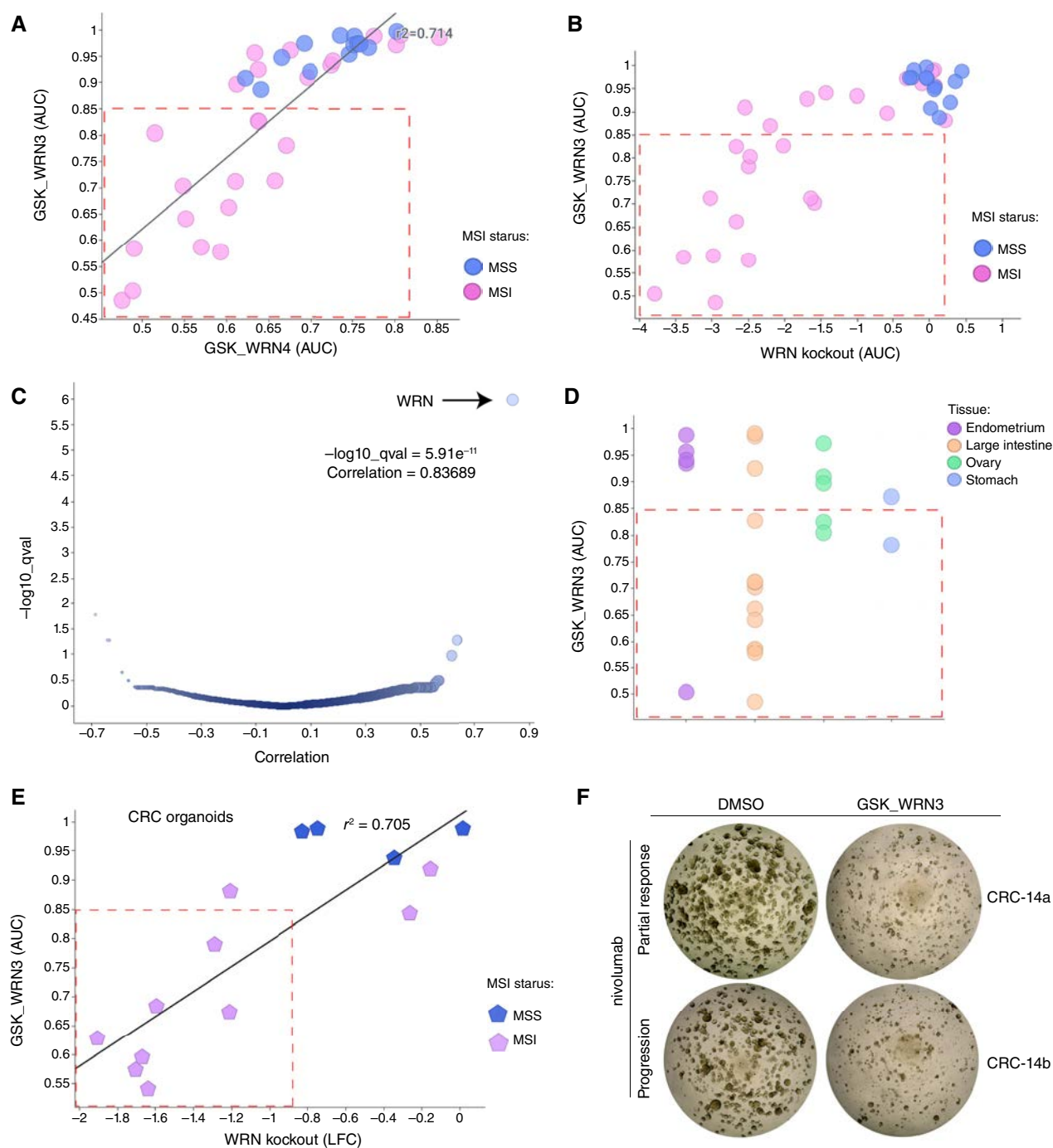


Figure 3. Selective inhibition of MSI cell growth by WRNis correlates with genetic inactivation. **A**, Sensitivity of 42 cell lines to GSK_WRN3 and GSK WRN4. MSI cancer cell lines (pink circles) exhibit a higher level of preferential inhibition than MSS models (blue), as delineated by the (red) dashed box (AUC < 0.85). **B**, Sensitivity of cell lines to GSK_WRN3 vs. WRN CRISPR knockout log-fold change (LFC). Drug sensitivity is measured as the area under the dose-response curve (AUC). **C**, Genome-wide CRISPR-Cas9 gene essentiality profiles correlated with GSK_WRN3 sensitivity in 39 cell lines. The correlation is plotted along the x-axis, whereas the $-\log_{10} P$ value is on the y-axis. **D**, The dot plot displays the AUC of GSK_WRN3 for different MSI-predominant tissues, with each dot symbolizing a cell line and colors indicating tissue type. **E**, A scatter plot correlating GSK_WRN3 activity in colorectal cancer organoids to WRN knockout LFC showcases a strong positive correlation. Color indicates MSI status. **F**, Representative images of colorectal cancer organoids that are refractory to immunotherapy, treated with either DMSO or 1.25 $\mu\text{mol/L}$ GSK_WRN3. Patient's clinical response to nivolumab is indicated. (Figure components were created with BioRender.com).

chromosome segregation and condensation; Supplementary Fig. S3H), consistent with cellular distress due to WRN loss and consequent DNA damage and cell-cycle arrest previously reported (16, 17, 37).

Collectively, these findings report a reactive fragment-based screening approach leading to the identification of covalent WRN helicase inhibitors with high selectivity *in vitro* and *in situ*.

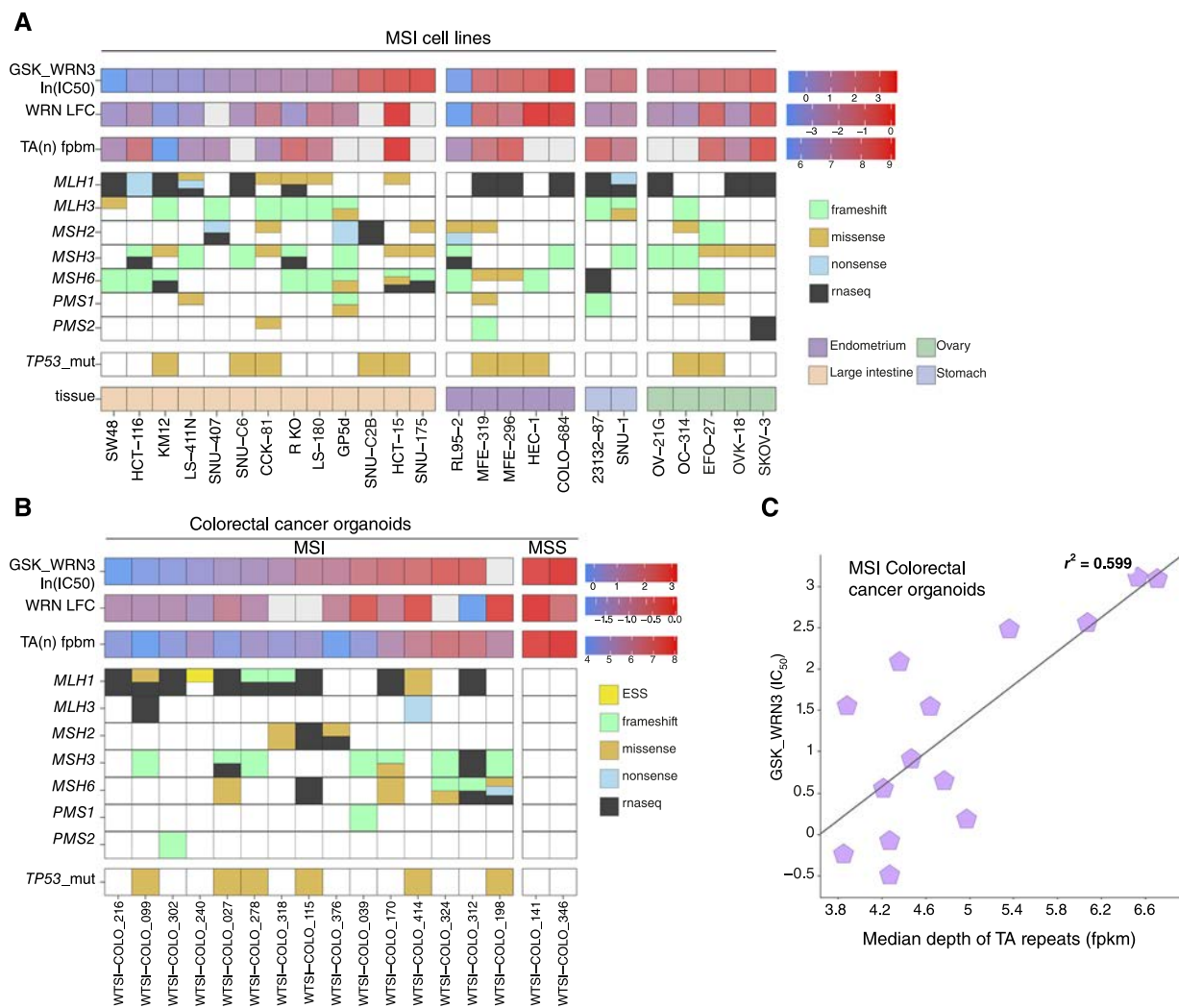


Figure 4. Sensitivity to WRN inhibition in MSI cancer models correlated with TA-repeat expansions and MMR gene alterations. **A**, Heatmap representing GSK_WRN3 sensitivity in MSI cell lines, measured by lnIC₅₀ values. The rows illustrate data for TA-repeat expansions TA_n (fpbm), WRN CRISPR dependency log-fold change (WRN LFC), and TP53 mutations (TP53_mut). The mutation status of MMR pathway genes (MLH1, MLH3, MSH2, MSH3, MSH6, PMS1, and PMS2) is displayed using color-coded squares for different mutation types: exon splice (yellow), frameshift (green), missense (orange), nonsense (cyan), and RNA sequencing (RNA-seq) confirmation (black). The tissue origin of each cell line is shown. **B**, Comparative heatmap for colorectal cancer organoids, segregating MSI and MSS profiles. The layout is similar to (A), with data for two MSS models included for comparison. **C**, Correlation of the IC₅₀ of GSK_WRN3 in colorectal cancer organoids to the median depth of “broken” TA repeats, as determined by coverage analysis from WGS. (Figure components were created with BioRender.com).

WRNi Selectively Inhibits MSI Cell Growth *In Vitro* and Phenocopies Genetic Inactivation

To assess the potency and selectivity of the WRNis, we evaluated their effect on *in vitro* viability in curated collections of cell lines and patient-derived tumor organoids. We initially screened GSK_WRN3, GSK_WRN4, and two putative WRNis previously reported, MIRA-1 and NSC617145 (21), across 42 selected cell lines. These were enriched in MSI models from MSI-predominant lineages and part of the Genomics of Drug Sensitivity in Cancer collection at the Sanger Institute. We observed a strong correlation in cell line sensitivity for GSK_WRN3 and GSK_WRN4 ($r^2 = 0.71$; Fig. 3A), and both drugs preferentially inhibited the growth of MSI cancer cell lines, while sparing microsatellite stable (MSS) models. In contrast, MIRA-1 and NSC617145 displayed poor efficacy and lack

of selectivity toward MSI models (Supplementary Fig. S4A). Notably, pharmacologic inhibition with GSK_WRN3 positively correlated with genetic WRN dependency by CRISPR screens in MSI-predominant lineages ($r^2 = 0.65$ MSI only; Fig. 3B). Furthermore, unbiased correlation analysis comparing genome-wide CRISPR-Cas9 gene essentiality profiles versus GSK_WRN3 sensitivity in 39 cell lines pinpointed WRN knockout as the top hit, confirming on-target compound activity (Fig. 3C). Sensitivity to WRNi was heterogeneous across MSI-prevalent tissues, with the top sensitive models consistently from colorectal cancer (Fig. 3D).

We next evaluated the sensitivity to WRNis using an independent cohort of 15 MSI and 4 MSS colorectal cancer patient-derived organoids from the Human Cell Model Initiative. Notably, we performed whole-genome CRISPR-Cas9

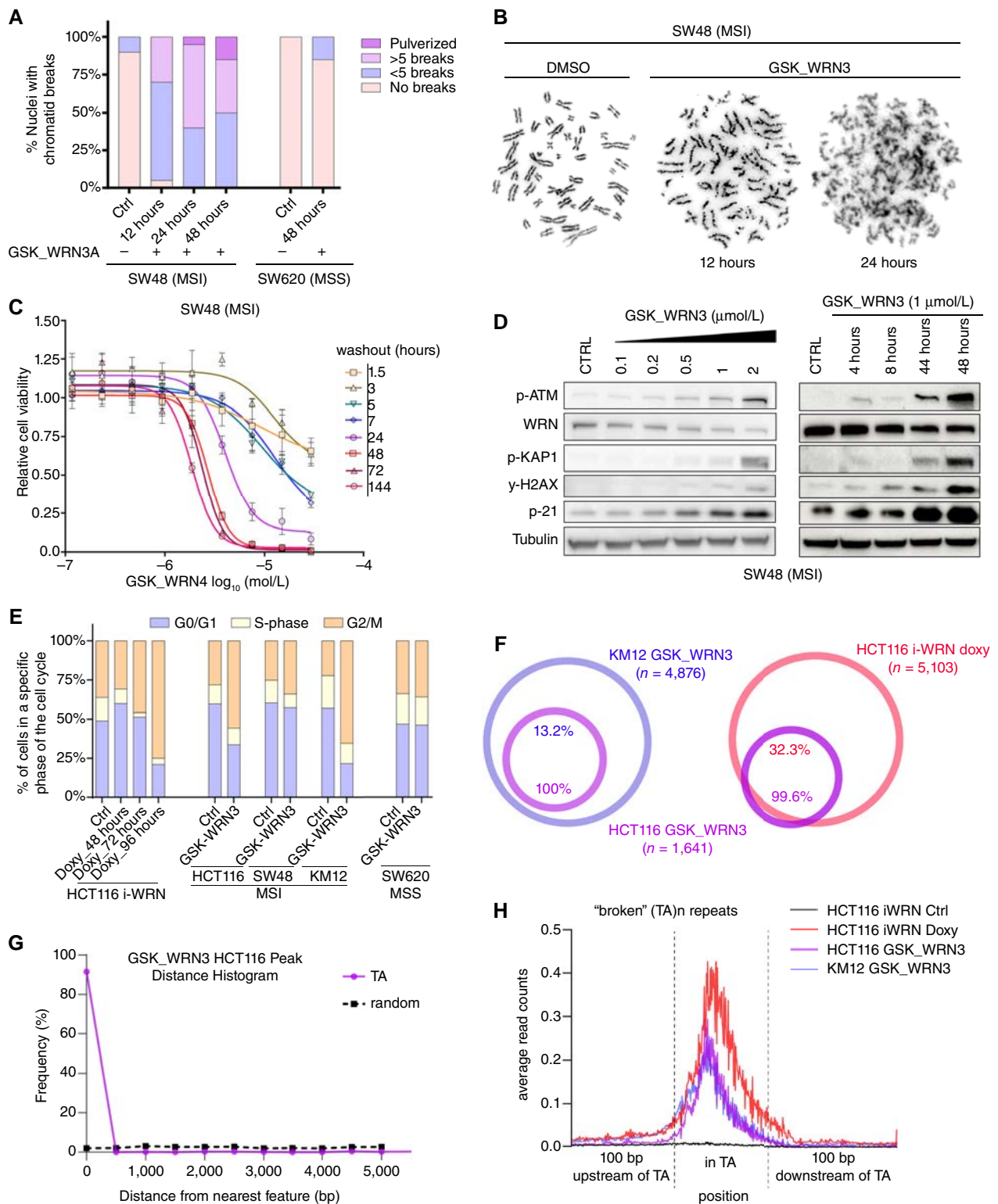


Figure 5. Chromosomal instability and DNA damage in MSI cells induced by WRN pharmacologic inhibition. **A**, Chromatid breaks in SW48 (MSI) and SW620 (MSS) cell lines after treatment with DMSO (ctrl) or GSK_WRN3 (2 $\mu\text{mol/L}$). Twenty metaphase spreads were analyzed per treatment. **B**, Representative images of SW48 metaphase spreads harvested after treatment with DMSO (12 hours) or GSK_WRN3 (12 and 24 hours). **C**, Time- and dose-dependent inhibition of SW48 cell growth by GSK_WRN4. SW48 cells were treated with 0.1–20 $\mu\text{mol/L}$ for 1.5, 6, 12, 24, 48, 72, or 144 hours. GSK_WRN4 was then washed out, and cell growth was assessed by cell counting over 72 hours. Data points represent the mean \pm SD of three independent experiments. **D**, Immunoblots of phospho-ATM, WRN, γ -H2AX, phospho-KAP1, and p21 in SW48 cells. Left, Post 48 hours treatment with GSK_WRN3, multiple concentrations as indicated. Right, Various time points posttreatment with 1 $\mu\text{mol/L}$ GSK_WRN3 (**E**). Cell-cycle phase distribution in HCT116 iWRN cells (*continued on following page*)

screens in 14 models to assess WRN genetic dependency, enabling direct comparison to pharmacologic WRN inhibition. In this set, sensitivity to WRNi displayed a gradient, with most models ($n = 7$) having apparent sensitivity. In contrast, a smaller number ($n = 3$) showed only partial sensitivity, whereas MSS models were fully resistant (Fig. 3E). There was a marked positive correlation between drug sensitivity and genetic knockout ($r^2 = 0.705$). Furthermore, GSK_WRN3 was effective in two additional organoid models from a primary (CRC-14b) and a metastatic (CRC-14a) lesion derived from a patient with sporadic colorectal cancer with a variable response to immunotherapy (Fig. 3F; Supplementary Fig. S4B). CRC-14b was derived from an immunotherapy refractory lesion and was previously characterized as WRN-addicted (20), confirmed here with pharmacologic inhibition. In summary, these results demonstrate that our WRNis phenocopy the effects of genetic WRN inactivation in MSI tumors. This provides pharmacologic proof of concept supporting WRN inhibition as a novel therapeutic approach for the treatment of patients with MSI-H cancers, including those resistant to standard-of-care therapies.

Determinants of WRNi Sensitivity in MSI Cancer Models

Taking advantage of our large cohorts of cell lines and organoids, we conducted comprehensive multiomics analyses on all models to evaluate molecular factors influencing WRNi sensitivity. This included estimating TA-repeat expansions through whole-genome sequencing (WGS; ref. 19, 20) and assessing *TP53* mutational status and alterations in MMR pathway genes, as all have been proposed as biomarkers of WRN inhibition sensitivity (20, 38). In cell lines from MSI-predominant lineages, GSK_WRN3 sensitivity correlated positively with expanded TA repeats ($r^2 = 0.63$ for all models and 0.56 for MSI-only models; Fig. 4A; Supplementary Fig. S4C and S4D). Notably, in colorectal cancer organoids, we observed a marked positive correlation between the extent of TA-repeat expansions and GSK_WRN3 IC₅₀ values ($r^2 = 0.72$ for all models and 0.6 for MSI-only models; Fig. 4B and C). Many sensitive cell lines and organoids have mutations in *TP53*, indicating the poor predictive value of *TP53* mutation as a negative biomarker of sensitivity (Fig. 4A and B). Similarly, WRNi sensitivity does not correlate with nutlin-3a sensitivity (active only in *TP53* wild-type cells) in cell lines or organoids ($r^2 = 0.1$ and 0.02, respectively; Supplementary Fig. S4E and S4F). As previously reported, alterations in *MLH1* showed a trend toward heightened sensitivity in colorectal cancer cell lines and organoids (20). Additionally, an independent cohort of 15 colorectal cancer MSI organoids underwent GSK_WRN4 sensitivity profiling,

VENTANA IHC, WES, and RNAseq analysis, revealing only a modest association of MMR alterations with WRN inhibition (Supplementary Fig. S4G).

In summary, these results offer preclinical evidence for TA-repeat expansions as biomarkers for improved stratification of patients with MSI suitable for treatment with WRNis.

WRN Pharmacologic Inhibition Induces Cytotoxic Chromosomal Instability and DNA Damage in MSI Cancer Cells

Genetic WRN inactivation results in chromosomal defects in MSI cancer cells (16, 17, 20). Therefore, we investigated the effects of treating MSI cells with GSK_WRN3 by analyzing the induction of DNA damage by karyotyping. We detected the presence of structural chromosomal aberrations selectively in MSI cells within 12 hours of treatment, characterized by a striking increase over time in the number of pulverized metaphases (Fig. 5A and B; Supplementary Fig. S5A). Subsequently, compound washout experiments were conducted, revealing that a 24-hour exposure to WRNi was sufficient to inhibit completely the growth of the SW48 cell line (Fig. 5C). In contrast, the MSS SW620 cell line remained largely unaffected (Supplementary Fig. S5B). GSK_WRN3, in a dose- and time-dependent manner, replicated the effects of genetic WRN inactivation by selectively degrading WRN and concurrently upregulating DNA damage response markers such as p-ATM, p-KAP1, p21, and γ -H2AX (Fig. 5D). Moreover, GSK_WRN3 induced G2 cell cycle arrest in MSI cells (Fig. 5E). Importantly, these effects were not observed in MSS SW620 control cells (Fig. 5E; Supplementary Fig. S5C).

WRN is required to resolve DNA secondary structures at expanded TA repeats in MMR-deficient cells. To identify the genomic sites of DNA double-strand breaks (DSB) in MSI cells treated with WRNis, we employed transferase-activated end ligation sequencing (TrAEL-seq; ref. 39). This method captures single-stranded DNA 3'-ends genome-wide and with base pair resolution. We used HCT116 cells engineered with an inducible sgRNA system for WRN targeting (i-WRN) as a positive control (15). Overall, pharmacologic inhibition of WRN and genetic loss of WRN showed strong concordance in DSB induction across cell lines. All of the DSB peaks ($n = 1,641$) observed in GSK_WRN3-treated HCT116 cells were fully recapitulated in GSK_WRN3-treated KM12 cells, whereas the 99.6% ($n = 1,637$) were detected in HCT116 i-WRN cells (Fig. 5F). In the GSK_WRN3-treated and i-WRN cells, nearly all the damage peaks were located in regions with TA repeats (Fig. 5G). We observed a marked increase in TrAEL-seq signal intensity within "broken" TA-dinucleotide expansion regions (Fig. 5H; Supplementary Fig. S5D; ref. 19), consistent with both WRN loss and pharmacologic inhibition inducing breaks at these regions.

Figure 5. (Continued) treated with doxycycline, and HCT116, SW48, and KM12 cells treated with 2 μ mol/L GSK_WRN3 for 24 hours. Data are representative of three independent experiments. **F**, The overlap of TrAEL-seq peaks in HCT116 (MSI) cells treated with GSK_WRN3, KM12 cells treated with GSK_WRN3, and HCT116 cells with CRISPR-mediated WRN knockout (i-WRN doxy). **G**, Frequency distribution showing the distance in base pairs (bp) of TrAEL-seq peaks in the GSK_WRN3-treated HCT116 cells from the nearest of 67,186 annotated TA-repeat tracts (magenta line) and from 70,000 random sites (dashed line). The x-axis is capped at 5 kb to emphasize the initial genomic spacing. **H**, TrAEL-seq signal metaplots in HCT116 iWRN cells. The figure compares signal variations across "broken" TA-repeats from van Wietmarschen and colleagues (19) under different conditions: DMSO (control), doxycycline (inducing sgRNA), and GSK_WRN3 in HCT116 and KM12 cells. The Y-axis shows average peak read counts, with the X-axis depicting relative peak positions: 100 bp upstream, within, and 100 bp downstream of TA repeats. (Figure components were created with BioRender.com).

Our data demonstrate that pharmacologic inhibition of WRN rapidly triggers hallmarks of DNA damage and chromosomal and cell cycle defects in MSI cells, and this is mediated through inducing DNA DSBs at expanded TA repeats, closely paralleling genetic WRN inhibition.

WRNi Potently Inhibits the Growth of MSI Models *In Vivo*, Including PDXs Refractory to Immunotherapy

To evaluate the antitumor efficacy of GSK_WRN4 *in vivo*, we established cell line xenografts from the MSI colorectal cancer cell line SW48 and the MSS colorectal cancer cell line SW620. Treatment with GSK_WRN4 via oral delivery led to dose-dependent tumor growth inhibition in the MSI SW48 xenografts, with tumor growth completely inhibited at the highest dosage, supported by favorable pharmacokinetics (Fig. 6A; Supplementary Fig. S6A). In contrast, GSK_WRN4 did not affect SW620 MSS xenograft growth, demonstrating high selectivity for MSI models (Fig. 6B). In addition, efficacy and selectivity were confirmed in xenografts from the LS411N (MSI) and HT-29 (MSS) cell lines, carrying TP53 and BRAF V600E mutations (Fig. 6C and D). Mice treated with GSK_WRN4 did not display significant body weight loss, even at the highest dose, reflecting a tolerable toxicity profile (Supplementary Fig. S6B).

To investigate the on-target pharmacodynamic effects of GSK_WRN4, we analyzed the modulation of DNA damage markers (p21, phospho-gamma H2AX, and p-KAP1) in the MSI xenografts. MSI xenografts treated with GSK_WRN4 had marked dose-dependent induction of all three markers, showing that GSK_WRN4 engages the intended molecular target *in vivo* and induces DNA damage (Fig. 6E–H and I; Supplementary Fig. S6C). Moreover, we found reduced proliferation marker Ki67 and increased caspase 3 staining, indicating GSK_WRN4 tumor growth inhibition and apoptosis (Fig. 6H and I). GSK_WRN4 induced DNA damage specifically in MSI-H tumors but not other tissues, demonstrating that the *in vivo* tumor growth inhibition by GSK_WRN4 at 300 milligrams per kilogram (mpk) is due to WRN helicase inhibition rather than off-target toxicity (Supplementary Fig. S6D). No significant modulation of DNA damage markers was detected in MSS xenografts (Supplementary Fig. S6E and S6F).

Morphologic and pathologic analysis of explanted tumors demonstrated that treatment with GSK_WRN4 led to a decrease in SW48 tumor cell density, accompanied by increased stroma and extracellular matrix deposition (Supplementary Fig. S6G). Additionally, the treatment led to enlarged and elongated nuclei in the tumors, similar to genetic ablation of WRN in MSI xenografts (15).

We next evaluated the efficacy of GSK_WRN4 in a PDX model from a patient with treatment-refractory MSI colorectal cancer, characterized by frameshift mutations in *MSH2*, *MSH3*, *MSH6*, and a pathogenic *TP53* missense mutation. The patient's cancer progressed despite undergoing the FOLFOX chemotherapy regimen (a combination of oxaliplatin, fluorouracil, and leucovorin), and exhibited stable disease without responding to bevacizumab and nivolumab (Fig. 6J). Remarkably, GSK_WRN4 treatment completely inhibited tumor growth in this immunotherapy-refractory PDX.

Together, these *in vivo* studies demonstrate that GSK_WRN4 exerts potent antitumor activity in MSI models while sparing MSS controls, inducing hallmarks of WRN inhibition-mediated DNA damage. The efficacy and on-target pharmacodynamic modulation support GSK_WRN4 as a therapeutic strategy for MSI cancers, including for the treatment of chemotherapy and immunotherapy-refractory tumors.

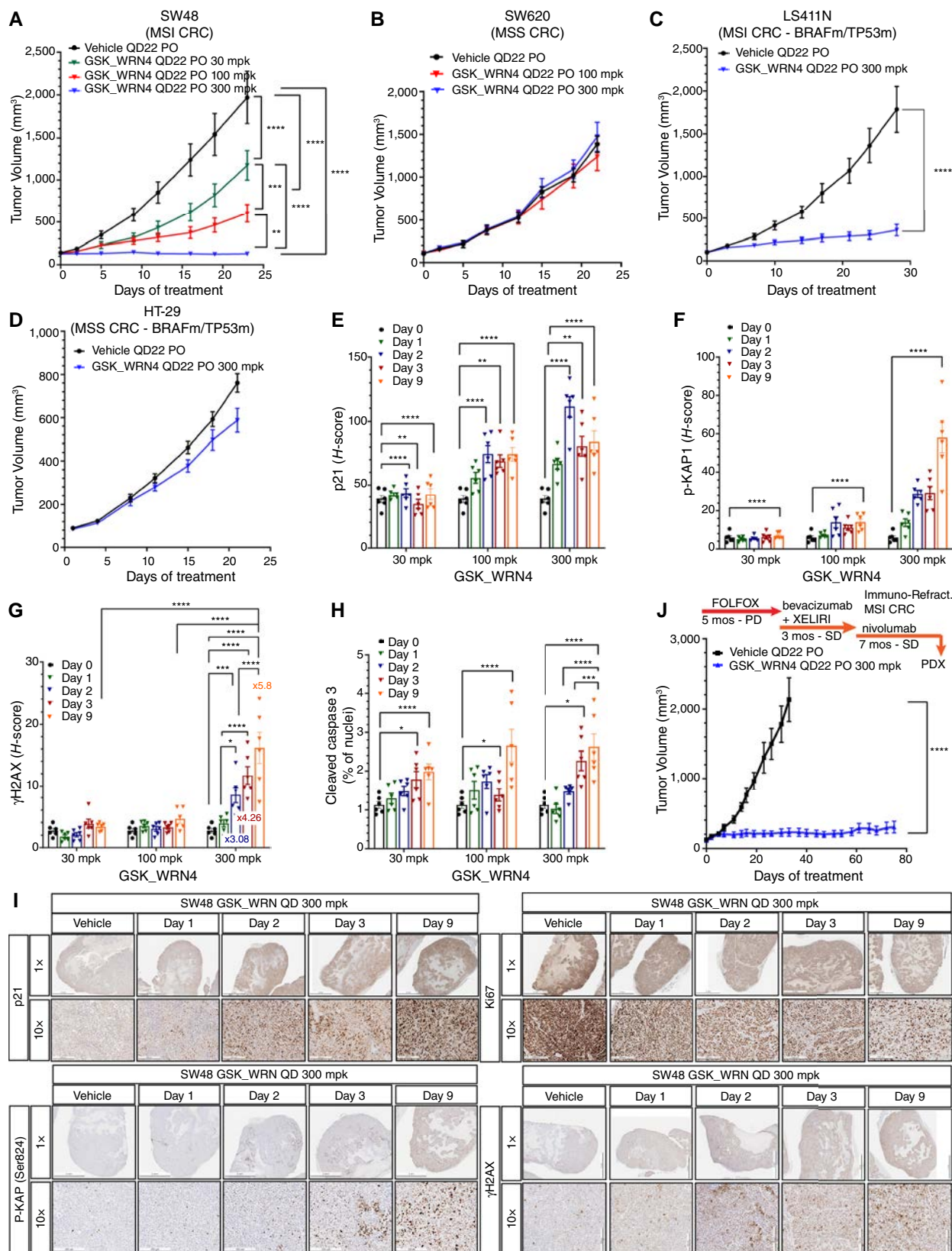
DISCUSSION

The concept of synthetic lethality can be exploited to develop medicines that selectively target critical vulnerabilities in cancer cells (40). This underlies the clinical success of PARP inhibitors for BRCA-deficient cancers (41, 42). Yet, the application of synthetic lethality in clinical treatments beyond the scope of PARP inhibition remains limited. The discovery of WRN-MSI synthetic lethality represents a new opportunity for synthetic lethal-based targeted cancer therapies. This study is the first detailed report of the biochemical, cellular, and *in vivo* activity of novel selective WRN helicase inhibitors and provides multiple lines of evidence to support the clinical development of WRNis.

We employed a CRISPR-Cas9 base editing platform to study the WRN-MSI synthetic lethal interaction. Key residues for survival were shared across cell lines and concentrated in the helicase domain, highlighting universal dependencies on particular WRN residues. This suggests inhibitors interfering with helicase enzymatic function could serve as broad-spectrum precision therapies, effective against diverse MSI tumors reliant on WRN.

We report the discovery and development of covalent WRNis, which have potent anticancer effects across various MSI models. Our inhibitors display remarkable on-target activity, demonstrating efficacy and selectivity across MSI-predominant cancer lineages. Notably, sensitivity was the greatest and most frequent in colorectal cancer models, with reduced and more variable sensitivity in other MSI-predominant tumor types. MSS cells were resistant to WRN inhibition, confirming the targeted efficacy and low toxicity of these inhibitors. Efforts to evaluate additional non-colorectal preclinical models would

Figure 6. Effects of GSK_WRN4 treatment on colorectal cancer cell lines and PDXs *in vivo*. **A–D**, Tumor volume measurements over time for xenograft of SW48, SW620, LS411N, and HT-29 colorectal cancer cell lines treated with vehicle or GSK_WRN4 at different doses (30, 100, and 300 mpk). **E–H**, Quantitative analysis of p21, p-KAP1, γ H2AX, and cleaved caspase 3 expression levels at days 0, 1, 2, and 9 posttreatment with GSK_WRN4, presented as *H*-score or percentage of positive cells. **I**, Representative IHC staining for p21, p-KAP1, γ H2AX, and Ki67 in SW48 tumors treated with vehicle or GSK_WRN4 (300 mpk) at various time points. **J**, Tumor volume measurements in an immunotherapy-refractory tumor xenograft derived from MSI colorectal cancer, treated with vehicle or GSK_WRN4 (300 mpk). Arrows denote the schematic timeline of clinical treatments, duration, and the corresponding tumor response before PDX establishment. *Note: Error bars represent SEM. Asterisks denote statistical significance compared to vehicle treatment (*, $P < 0.05$; **, $P < 0.01$; ***, $P < 0.001$; ****, $P < 0.0001$). *H*-score, a combined score of staining intensity and percentage of positive cells; PD, progressive disease; PO, per os indicating oral administration; QD, per daily; SD, stable disease. (Figure components were created with BioRender.com).



Downloaded from <http://aacrjournals.org/cancerdiscovery/article-pdf/14/8/1457/347339/ed-24-0052.pdf> by guest on 03 April 2025

deepen our understanding of sensitivity factors in the setting of MSI and potentially widen the efficacy of WRNis to additional cancer types.

We perform the first analysis of biomarkers of response to WRN inhibition in a large set of preclinical models. Our results do not support *TP53* mutations conferring resistance to WRNis (38), which is consistent with recent genetic studies (43). Notably, we validate TA-repeat expansions as significant sensitivity indicators for WRNis in colorectal cancer models, an important indication for patient selection strategies using specific molecular or genetic markers. Although reliant on WGS data and needing further refinement, this biomarker could be used to refine patient stratification. We noted a positive correlation between *MLH1* alterations and WRN sensitivity, although specific MMR alterations do not conclusively predict sensitivity.

There is a strong correlation between WRN genetic essentiality and sensitivity to pharmacologic inhibition, highlighting the compounds' specificity and validating the utility of the cancer dependency map (44) in identifying targets that are therapeutically exploitable. In addition, WRN pharmacologic inhibition effectively mimicked genetic knockouts, robustly inducing DNA damage both *in vitro* and *in vivo*. Our selective WRNis, distinct from genetic tools like CRISPR knockout or RNAi, allow for precise and tunable inhibition of WRN helicase function. In-depth *in vitro* characterization of the response dynamics indicates that pulsing with WRNis can effectively induce significant DNA damage and cytotoxicity. This understanding can inform drug administration regimens during clinical development to maximize therapeutic efficacy.

We comprehensively analyzed 31 patient-derived organoids with WRNis and evaluated WRN gene dependence for 14 models. This new dataset improves our understanding of WRN essentiality, which was previously largely confined to conventional 2D cancer cell line-based dependency maps, offering deeper insights into the effectiveness of WRN-targeted drugs and the determinants of drug sensitivity in 3D patient-derived preclinical models. In addition, we thoroughly validated the efficacy of WRNis *in vivo*, demonstrating their ability to selectively halt the growth of MSI tumors without causing toxicity, as they induce DNA damage only in cancer cells. The activity of WRNis on preclinical models derived from treatment-resistant tumors, including immunotherapy, support the use of WRNis for patients with treatment-refractory disease either as monotherapy or as combination therapies (20).

In conclusion, this study represents an important step forward in the development of precision medicine for MSI cancers. By integrating genomic editing approaches with fragment-based drug development, new potent and selective pharmacologic WRN helicase inhibitors targeting the WRN-MSI synthetic lethal interaction were successfully developed. These compounds consistently and effectively impaired viability across diverse MSI models, expanding therapeutic options. These findings validate pharmacologic WRN inhibition as a promising precision therapy for MSI malignancies harboring this vulnerability and support the clinical development of small-molecule inhibitors targeting WRN helicase for treating patients with MSI tumors.

METHODS

Cell Models

Cell lines and organoids used in this study were curated from the Genomics of Drug Sensitivity 1,000 cell line collection and are annotated in the Cell Model Passports database (<https://cellmodelpassports.sanger.ac.uk/>; ref. 45). Cell lines were maintained in their original culturing conditions according to supplier guidelines. Cells were supplemented with 10% FBS, 2 mmol/L L-glutamine, and antibiotics (100 U/mL penicillin and 100 mg/mL streptomycin) and grown at 37°C and 5% CO₂ air incubator. All cell models tested negative for *Mycoplasma* in two complementary methods, MycoAlert (Lonza) and EZ-PCR (Biological Industries). Models were profiled using a panel of 94 single-nucleotide polymorphisms (Fluidigm, 96.96 Dynamic Array IFC). A minimum of 75% of SNPs was required to match the reference profile for a sample to be positively authenticated. In addition, short tandem repeat profiles were generated and matched to those provided by the cell line repositories. Models were maintained in the lab for 36 days on average (maximum 60 days), and all experiments were conducted within this period. Source of cell lines and organoids used in this study are listed in Supplementary Table S3.

Compounds, Drug Screening, and Dose-Response Curve Fitting

The compounds were sourced from commercial vendors or provided by GSK. DMSO-solubilized compounds were stored at room temperature in low humidity (<12% relative humidity) and low oxygen (<2.5%) environments using storage pods (Roylan Developments). Screening of cancer cell lines and organoids available at the Sanger Institute was performed using both single treatments and combinations. Compounds were screened at 12 concentrations spanning a 2,048-fold range with a twofold dilution series. Cells were transferred into 384-well assay plates in 40 µL (cell lines) or 60 µL (organoids) of their respective growth medium using Multidrop Combi (Thermo Fisher Scientific) dispensers. Each model's seeding density was optimized prior to screening to ensure that each cell line was in the exponential growth phase at the end of the assay. Six cell densities were tested with a twofold dilution step; each density was dispensed into 48 wells of a single 384-well assay plate and incubated for 96 hours. Cell number was quantified using CellTiter-Glo 2.0 (Promega). The maximum density tested was 3,200 cells per well. Assay plates were incubated at 37°C in a humidified atmosphere at 5% CO₂ for 24 hours and then dosed with the test compounds using an Echo555 (Labcyte). The final DMSO concentration was typically 0.1%. The assay plates were incubated after dosing with compounds, and the drug treatment duration was 72 hours. CellTiter-Glo 2.0 (Promega) was added, 13.5 µL for cell lines or 20 µL for organoids, to measure cell viability. Each assay plate was incubated at room temperature for 10 minutes before quantification of luminescence using a Paradigm (Molecular Devices) plate reader. To estimate cell growth throughout drug treatment, an additional undrugged control plate was generated, and cell viability was measured at the time of drug treatment. These plates are referred to as a "day = 1" and were repeated each time a cell line was screened. All screening plates contained negative control wells (untreated wells, *n* = 6; DMSO-treated wells, *n* = 62) and positive control wells (medium-only wells, *n* = 12; Staurosporine-treated wells, *n* = 8; and MG-132 treated wells, *n* = 8) distributed across the plates. These control wells were used to evaluate defined quality control criteria, including the coefficient of variation (CV) and Z-factor calculated as previously described (46). A maximum threshold of 0.23 was applied to the CV, and Z-factors were required to exceed a minimum threshold of 0.3. Where a cell line was sensitive to both positive controls, it had to pass Z-factor thresholds for both positive controls. Plates that did not meet these requirements were excluded from the study.

Luminescence readings were converted to cell viabilities by normalizing with reference to the DMSO-treated wells and the positive controls (viabilities of 1 and 0, respectively). Dose-response curves were then fitted to the drug-treated wells using a nonlinear mixed effect model (47) to obtain IC₅₀ estimates. Curves with a root mean squared error of greater than 0.3 were excluded from further analysis.

Organoid Culture Techniques, CRISPR/Cas9 Genome Screening, and Drug Efficacy Testing

The maintenance of organoids and transduction of a genome-wide sgRNA library were adapted from previously reported protocols (15, 20, 48, 49). For drug efficacy testing of the CRC-14a and CRC-14b models, organoids were dissociated into single cells and seeded into each well of a 96-well plate with a 5 μ L droplet of 80% BME solution, overlaid with organoid media. Approximately 1.5 to 2.5 \times 10³ cells per well were cultured. The next day, variable concentrations of the relevant drug were added in triplicate for each model. Cell growth was monitored over 7 to 10 days, followed by imaging using an EVOS Cell Imaging System (Thermo Fisher Scientific).

Cell Line Engineering for Base Editing

We introduced base editing machinery into cells by cotransfecting with FuGENE HD (Promega), using a plasmid encoding Cas9 and a guide RNA (gRNA) targeting the CLYBL locus (5'-ATGTTGGAAGGATGAGGAAA-3'), alongside a plasmid with tet-ON base editor, blasticidin resistance, and mApple expression cassettes within CLYBL homology arms as recently reported (31). To enhance homologous recombination rates, cells were pre-incubated overnight with 1 μ Mol/L DNA-PK inhibitor AZD7648. Transfected cells were selected using 10 μ g/mL blasticidin (Thermo Fisher Scientific) for 4 days, followed by 5 μ g/mL maintenance. Cell pools were further refined via FACS based on mApple expression. Base editing efficiency was evaluated using BE-FLARE (50). For detailed screening, clonal lines of BE3.9max NGN and ABE8e NGN were utilized.

CRISPR-Cas9 Base Editing Screens

Our base editing cell lines were established following the method outlined in a previous study (31). In brief, we utilized CRISPR-Cas9 and homology-directed repair to insert doxycycline-inducible CBE or ABE NGN base editors at the CLYBL safe-harbor site. Base editing cell populations were selected using blasticidin and mApple (FACS). Base editing activity was assessed using BE-FLARE (for CBE) or a GFP stop codon reporter (for ABE). We conducted base editing screens with gRNA representation of 1,000-fold, utilizing viral doses that resulted in 30% to 50% cell infection. Postinfection, cells were selected with puromycin for 4 days. Five days postinfection, a baseline (T₀) pellet was collected. Base editing was induced by administering doxycycline (1 μ g/mL) for 3 days. This was followed by a 10-day selection phase, during which cells were maintained in culture (a minimum of 15 million cells in three-layer flask) and split regularly. Each screen was independently replicated 2 times on separate days for consistency. For DNA analysis, cell pellets were processed to extract DNA, and the gRNA cassette was amplified through PCR. This was done in parallel to maintain library diversity. Post-column purification, PCR products were indexed and sequenced on the Illumina HiSeq 2500, using 19 bp single-end sequencing and a custom primer.

gRNA Library and Screen Data Analysis

To develop control gRNAs for base editing, we employed SpliceR (51), selecting the top three gRNAs using a unique metric: the product of the cDNA disruption score and the sum of ABEScore and CBEScore. For gRNAs targeting WRN exonic regions, the BEestimate tool (currently in preparation for submission and available at <https://github.com/CansuDincer/BEestimate>) was employed. Oligonucleotides, designed

and obtained from Twist Biosciences, underwent PCR amplification. Subsequently, these amplified products were seamlessly integrated into the BbsI-cleaved pKLV2-U6gRNA (BbsI)-ccdB-PGKpuro2ABFP-W lentiviral vector using the Gibson Assembly method provided by New England Biolabs (49). Following assembly, the resulting libraries underwent ethanol precipitation for condensation and were introduced into Endura electrocompetent cells (Lucigen) via electroporation. This step was meticulously performed in parallel to ensure the consistency of the library. The transformed cells were cultivated in Luria-Bertani medium supplemented with 100 μ g/mL ampicillin at 30°C grown overnight in the shaking incubator. Lentiviral vectors, along with packaging plasmids psPax2 and pMD2.G (Addgene), were transfected into 80% confluent HEK293 cells using Lipofectamine LTX (Gibco) at the specified ratio: 7.5 μ g of lentiviral vector (library plasmid DNA), 18.5 μ g of psPax2, and 4 μ g of pMD2.G per 15 cm dish. Viral particles were harvested from the media's supernatant 72 hours posttransfection, subsequently filtered, and stored in a frozen state.

For analyzing screen results and annotating gRNAs, we employed BEestimate. We assumed a wild-type genome as the baseline, disregarding specific SNPs or SNVs in the two cancer cell lines. We normalized read counts to reads per million, adding a pseudo-count for calculation purposes. We averaged reads per million values from replicates for consistent gRNA analysis. Average log₂fold-change values were calculated and z-scores were derived by normalizing these values against their SD. RNAs with fewer than 100 reads in the initial samples were also discarded. WRN syndrome registry variants were obtained from Friedrich and colleagues (52) and the Werner Syndrome Mutational Database <https://www.pathology.washington.edu/research/werner/database/>. Alphamissense pathogenicity score and class were downloaded from the Alphamissense manuscript supplementary information (30). Clinical variants associated with WRN syndrome were downloaded from the ClinVar database <https://www.clinicalgenome.org/data-sharing/clinvar/>. For both ClinVar and WRN syndrome registry variants, only missense mutations were used for the analysis.

WRN C727 Mutation Knock-in

CRISPR-mediated homologous recombination was employed to introduce single amino acid substitutions to Cys727 on WRN in SW48 cells. To this end, sgRNA is designed to include crRNA 5'-AAUCCUCAGAUCACCUGUAC-3'. Cys727Ala and Cys727Ser were introduced using designed homologous recombinant templates: Cys727Ala (gcacttactgctactgcaagtcttcaatccgggaagacattgacgttgcttaaatctgaga aaCccGcaAatTacGGCTacc ggttttgatcgcaaacctgtattagaagttaggcgcaaaaacagggaaatctct); Cys727Ser (gcacttactgctactgcaagtcttcaatccgggaagacattgacgtttgcttaaatctgaga aaCccGcaAatTacGAGTacc ggttttgatcgcaaacctgtattagaagttaggcgcaaaaacagggaaatctct). sgRNA and single-stranded oligonucleotides were both synthesized at Integrated DNA Technologies. SW48 cells were maintained in RPMI 1640 + 10% FBS cell culture media and passaged with standard cell culture techniques. CRISPR-mediated knock-in was performed with electroporation of Cas9/sgRNA RNP mixture. Specifically, mix 2 μ L Cas9 protein (Integrated DNA Technologies #1081061, 10 μ g/ μ L) with 0.5 μ L sgRNA (400 μ Mol/L) and incubated at room temperature for 15 minutes to allow RNP complex to assemble. A resuspension of 4 \times 10⁵ SW48 cells in 20 μ L electroporation buffer [prepared according to Lonza's manual for Amaxa SF cell line 4D-nucleofector X Kit S (32 RCT), Lonza#V4XC-2032] was mixed with 1 μ L of 100 nmol/L ALT-R electroporation enhancer (Integrated DNA Technologies, ALT-R HDR Enhancer V2). When the RNP mix was ready, the cell suspension was mixed in electroporation buffer with RNP mix in one well of the electroporation chamber from the SF kit. 1 μ L of single-stranded oligonucleotides (100 μ Mol/L) was added to the cell/RNP mix and electroporated with K562 cell line protocol on the Amaxa 4D-Nucleofector

X unit. Cells were transferred to fresh media containing 1 $\mu\text{mol/L}$ of ALT-R electroporation enhancer V2 immediately after electroporation and cultured for 24 hours. The cell media was replaced with fresh media 24 hours after electroporation.

Genomic DNA of electroporated cells were extracted with Zymo DNA extraction kit (Zymo quick-DNA 96 kit; Zymo Research, #D3012). A total of 50 ng of genomic DNA was used for PCR amplification of edited genomic region. A 50- μL PCR reaction was set-up per sample: 25 μL 2 \times Phusion Master Mix, 1 μL forward and reverse primer mix (25 $\mu\text{mol/L}$ each), 1.5 μL DMSO, add H_2O to 50 μL . The primer sequences used for PCR amplification were forward (GACATGTTGGGAATGAATGAGC) and reverse (AAGAAATGGC TGCAGATCCTGA). PCR products were purified with Zymo PCR purification (ZR DNA sequencing clean up kit; Zymo Research, #D4051). Purified PCR samples were sequenced using Sanger Sequencing service at Genewiz. Knock-in efficiency was performed using Synthego ICE analysis tool (<http://ice.synthego.com>). Cells with sequencing verification of knock-in efficiency were treated with GSK_WRN3 and GSK_WRN4, with top dose of 30 $\mu\text{mol/L}$ and 1:3 dilution down to 4.6 nmol/L. Compounds were dispensed on HP D300e dispenser. 2×10^3 cells per well were cultured in 96-well assay plate (ThermoScientific, #136102) in 100 μL volume with compound for 4 days. Cell viability was measured by adding 50 μL CellTiter-Glo One Solution Assay (Promega, #G8642). CTG (CellTiter-Glo) readings were normalized to the DMSO wells, curve fitted, and plotted in GraphPad Prism 9.0.

Karyotype Analysis with Human Multiplex FISH Probes

Cells were harvested 12, 24, or 48 hours posttreatment with GSK_WRN3 or DMSO, following a modified standard protocol for metaphase preparation. In brief, cells in T150 flasks were treated with 0.1 g/mL colcemid (KaryoMax Colcemid Solution in PBS, Thermo Fisher Scientific) for 1.5 hours. TrypLE Express Enzyme (Thermo Fisher Scientific) was used for dissociating adherent cells into a single-cell suspension, which was then pelleted and resuspended in 0.56% KCl hypotonic solution for 12 to 14 minutes, followed by fixation with Carnoy's fixative (3:1 methanol:acetic acid). FISH analysis was performed according to previously reported methods (53). Metaphase slides were prepared, fixed in acetone (Sigma-Aldrich) for 10 minutes, and baked at 62°C for 30 minutes. Slides underwent alkaline denaturation (0.5 mol/L NaOH and 1.0 mol/L NaCl) for 7.5 to 8 minutes, followed by washes in 1 mol/L Tris-HCl (pH 7.4) and 1 \times PBS. Dehydration was achieved through a 70%, 90%, and 100% ethanol series. The 24-color human multiplex FISH probe mix was denatured and applied to the slides, with hybridization at 37°C for two nights. Posthybridization washing included 2 \times SSC at 37°C, a stringent wash in 0.5 \times SSC at 75°C, and rinses in 2 \times SSC with 0.05% Tween-20 (VWR) and 1 \times PBS. Slides were mounted in Vectashield Vibrance Antifade Mounting medium with DAPI (VectorLabs). Imaging was done using an Axio Imager D1 microscope with appropriate filters, capturing digital images via SmartCapture software (Digital Scientific). Twenty randomly selected metaphase cells were karyotyped and analyzed, focusing on chromatid and chromosome breaks and complex rearrangements, using the SmartType Karyotyper (Digital Scientific) based on multiplex FISH and DAPI banding patterns.

Multomics Analysis

Mutations in MMR pathway genes were downloaded from The Cell Model Passport or Dependency Map (DepMap) websites. Genetic analysis was performed as previously described (20). To identify which MMR pathway gene displayed altered gene or protein expression, we computed the Z-score by gene across all the cell lines (or organoids) in the respective data set and considered genes with Z-score or normalized values less than -2 to identify genes downregulated in a particular sample. WRN dependency was obtained mining essentiality data obtained from multiple sources: Project Score

(<https://score.depmap.sanger.ac.uk/>) and Dependency Map (DepMap; <https://depmap.org/portal/>) websites. For TA dinucleotide repeat expansion analysis, WGS data for cancer cell lines were downloaded from SRA study SRP186687.

Western Blot

Immunoblot was conducted to verify WRN depletion and DNA damage in cells treated with various concentrations of WRNi. For the blots, 4 to 8×10^6 cells were cultured in 10 cm dishes and treated with GSK_WRN3 or DMSO. Cells were lysed at 4, 8, 24, 48, and 72 hours posttreatment using 100 to 150 μL RIPA buffer with proteinase inhibitors. The lysate concentration was quantified via the BCA Assay. Each sample, containing 20 to 30 μg of lysate, was subjected to SDS-PAGE on a 4% to 12% Bis-Tris gel (Invitrogen) and then transferred to a polyvinylidene difluoride membrane. After blocking with 5% milk in Tris-buffered saline with Tween 20 (TBST), membranes were incubated overnight with primary antibodies: anti-WRN (Cell Signaling Technology, 4666, 1:1,000), anti-P-ATM (Abcam, ab81292, 1:1,000), anti-KAP1 (A300-767A.M, 1:1,000), anti-P-Histone H2AX (NB100-384, 1:1,000), anti-P21 (96109520, 1:1,000), and anti- β -tubulin (Sigma-Aldrich, T4026, 1:5,000) as a loading control. Blots were washed and incubated with an anti-Rabbit IgG HRP-linked secondary antibody (GE Healthcare, #NA931V-ECL HPR) for 1 hour at room temperature. Following another wash in TBST, the signal was amplified with SuperSignal Dura for visualization. Precision All Blue Plus Protein Standards (Bio-Rad, cat. 1610373) served as a molecular weight marker.

Cell-Cycle Analysis

We employed propidium iodide (PI) staining to evaluate cell viability. Cells were harvested using standard protocols and washed in PBS. The cell pellet was subsequently fixed in cold 70% ethanol and stored at 4°C for over 1 hour, with overnight fixation being optimal for enhanced data resolution. Following fixation, cells were washed 2 times in PBS and centrifuged at 1,200 rpm for 5 minutes, after which the supernatant was discarded, taking care not to disturb the loose pellet. The cell count was determined for each treatment group before staining. For staining, 500 μL of PI solution at a concentration of 1×10^{-6} cells/mL was added to the cell pellet, followed by incubation for more than 1 hour at room temperature or overnight at 4°C. The PI solution was prepared with Triton X-100 at 0.1% (v/v), RNase A at a final concentration of 50 $\mu\text{g/mL}$, and PI at 25 $\mu\text{g/mL}$, topped up to 50 mL with PBS. Postincubation, cells were analyzed by flow cytometry to determine viability based on PI uptake.

TrAEL-seq for DSB Mapping

For TrAEL-seq, 2 to 3 million cells were seeded in T150 flasks. Two days later, these cells were treated with GSK_WRN3 for 24 hours or with doxycycline for 72 hours. Cells were harvested and counted 24 hours post-treatment. 1 to 2×10^6 cells per treatment were washed with PBS, centrifuged, and resuspended in 1 mL of cold L Buffer (100 mmol/L EDTA pH 8, 10 mmol/L Tris pH 7.5, 20 mmol/L NaCl), before embedding in agarose for DNA extraction. DNA ends were tailed with ATP and ligated to adapters carrying in-line indexes, then pooled and processed into a single TrAEL-seq library as described (39). Libraries were sequenced on an Illumina NextSeq 500 as High Output 75 bp Single End by the Babraham Institute Next Generation Sequencing facility, and then reads were trimmed, deduplicated, demultiplexed into individual libraries, and mapped to GRCh38 by the Babraham Institute Bioinformatics Facility using scripts available at <https://github.com/FelixKrueger/TrAEL-seq>.

Analysis of TrAEL-seq Data

Mapped reads were imported into SeqMonk v1.48 (<https://www.bioinformatics.babraham.ac.uk/projects/seqmonk/>) and truncated to one nucleotide at the 5'-end, representing the last nucleotide 5' of

the strand break. No normalization between datasets was performed as all data came from multiplexed libraries and should be quantitatively comparable. Peak finding was performed in each sample using MACS implemented in SeqMonk (macs2 - nomodel - tsize 100 - P value $1e^{-15}$ - keep-dup), and distances from MACS peaks to nearest TA tract or random sites calculated using Distance to Feature Quantitation. For the metaplot, strand-specific read counts were performed at 1 nT resolution over broken TA tracts defined in van Wietmarschen and colleagues (19) ± 100 bp using the Quantitation Trend Plot function. Final graphs were plotted using GraphPad Prism 10.1.1.

Reactive Fragment Intact-Protein LC/MS Screen

Fragment-based covalent ligand screening was performed as previously reported (34). Briefly, recombinant WRN helicase domain (500–946) was diluted to 0.5 μ L in 25 mmol/L HEPES, 50 mmol/L NaCl, pH 7.5 buffer. Protein solution (10 μ L) was added to the reactive fragment library (10 nL of 20 mmol/L DMSO stock) in a 384-well plate. The plate was centrifuged at 1,000 rpm for 1 minute then sealed and incubated at 21 °C for 24 hours. After 24 hours, LC/MS-grade H₂O (10 μ L) was added to all wells. The plate was centrifuged at 1,000 rpm for 1 minute, sealed, and then transferred to LC/MS plate hotel. Samples were measured using an Agilent G230B time-of-flight accurate Mass Series mass spectrometer interfaced with an Agilent 1290 infinity II series column oven (G7116B) and an Agilent 1290 infinity II series liquid chromatography high-speed binary pump (G7120A). Protein samples were injected using an Agilent 1290 infinity II series multisampler with dual needles with a 2 μ L injection volume. Chromatography was carried out on an Agilent Bio-HPLC PLRP-S (1,000 Å, 5 μ m \times 50 mm \times 1.0 mm, PL1312-1502) reverse phase HPLC column at 70 °C. The sample was eluted at 0.5 mL/minutes using a gradient system from solvent A [water, 0.2% (v/v) formic acid] to solvent B [acetonitrile, 0.2% (v/v) formic acid] according to the following conditions: at 0.00 minutes, the percentage of solvent B is 20%. This remains the same at 0.60 minutes. At 0.61 minutes, it increases to 50%, and by 1.00 minute, it reaches 100%. The percentage of solvent B stays at 100% until 1.20 minutes, after which it decreases back to 20% at 1.21 minutes. The eluent was injected directly into an Agilent time-of-flight mass spectrometer (G6230B) using a dual AJS ESI source and scanning between 600 and 3,200 Da with a scan rate of 1.2 seconds in positive mode. Data acquisition was carried out in 2 GHz Extended Dynamic Range mode. Spectra were processed using MassHunter BioConfirm software 10.0 (Agilent) with the maximum entropy method employed. The total ion chromatograms were extracted and the summed scans were deconvoluted over an *m/z* range of 49,000 to 53,000 Da.

The deconvoluted spectra were exported as .csv files and analyzed using an R script to generate PDF files of the spectra. The median of the protein-only controls were subtracted from the sample spectra to remove baseline signal. The peak height for unmodified protein and protein modified by reactive fragments were recorded and used to calculate percentage modification. In this study, we utilized a synthesis method for WRNis as described by Adams and colleagues, Patent No. WO2023062575 A1 (54).

Covalent Modification Site Identification by Tandem MS

GSK_WRN1 (20 μ mol/L) was incubated with WRN helicase domain (2 μ mol/L) and incubated at 21 °C for 24 hours. The sample was separated by SDS-PAGE to remove excess unbound compound. Gels were stained with colloidal Coomassie InstantBlue, and bands corresponding to WRN were excised, reduced with 10 mmol/L TCEP (65 °C, 30 minutes), and alkylated with 10 mmol/L iodoacetamide (21 °C, 30 minutes, dark). Samples were digested with trypsin (Promega) 1:10 E:S (37 °C, 16 hours) in 100 mmol/L ammonium bicarbonate. After the removal of the supernatant, peptides were extracted using

acetonitrile. Combined supernatants were concentrated in a SpeedVac centrifuge and acidified (0.1% formic acid and 0.05% trifluoroacetic acid) before injection into the LC-MS/MS system. Digested samples were injected on an Easy-nLC 1000 UHPLC system (Thermo Scientific). The nanoLC was interfaced to a Q-Exactive Hybrid Quadrupole-Orbitrap Mass Spectrometer (Thermo Scientific) and separated on a 25 cm \times 75 μ m, 2 μ m particles, PepMap C18 column (Thermo Scientific) using a 50 minutes gradient of 2% to 38% acetonitrile, 0.2% formic acid and a flow rate of 300 nL/minutes. LC/MS-MS-based peptide sequencing was performed using data-dependent analysis. Uninterpreted tandem MS spectra were searched for peptide matches against the sequence of WRN helicase domain using Mascot (v2.6.0) software with a 5 ppm mass tolerance for peptide precursors and 20 mDa mass tolerance for fragment ions. Raw files were searched using trypsin as the enzyme with up to two missed cleavages, and the variable modifications, carbamidomethylation on cysteine and oxidation on methionine, were allowed. Masses corresponding to GSK_WRN1 were allowed as variable modifications on cysteine. MS/MS spectra were manually validated and annotated.

WRN Unwinding Assay

Functional WRN unwinding activity was measured using a fluorogenic plate based 384-well assay configured to measure the separation of labeled double-stranded DNA substrate. Compounds were dosed out in neat DMSO with a 1:3 serial dilution scheme. 100 nL of compound was stamped into Greiner low volume black assay plates (Greiner, Cat #784076) using the Echo Acoustic Dispenserto generate assay ready plates. All solutions were prepared in assay buffer (25 mmol/L TRIS (pH 8.0), 5 mmol/L NaCl, 2 mmol/L MgCl₂, 1 mmol/L dithiothreitol (DTT), 0.05% BSA) for this 10 μ L low volume reaction. To prepare the solutions, a 2 \times WRN enzyme cocktail was made containing 200 pmol/L of recombinant full-length WRN protein (1–1,432). A 2 \times substrate cocktail was made to consist of both 200 μ M ATP (any ultra-pure ATP sample) and 12 nmol/L of the fluorescent quenched labeled double-stranded DNA oligomer [IDT Custom synthesis; 5'-SIABkFQ (SEQ ID NO. 1)/GCA CTG GCC GTC GTT TTA CGG TCG TGA CT-3' (SEQ ID NO. 2): 5'-TTT TTT ACT TAA CGA CGG CCA GTG C (SEQ ID NO. 3)/36-TAMTSP/-3' (SEQ ID NO. 4)]. To start the reaction, 5 μ L of assay buffer was added to a single column to serve as the low control. Following this, 5 μ L of 2 \times WRN enzyme was added in all wells except the buffer low control wells. The reaction plate was covered and incubated at ambient temperature for 4 hours to allow for time-dependent inhibition if it existed. After 4 hours, the addition of 5 μ L of 2 \times -ATP/DNA substrate cocktail was added across all wells of the assay plate. This initiated the reaction, as the plate was incubated at ambient temperature for 60 minutes for the unwinding reaction to occur. A 10 mmol/L EDTA solution was prepared and added at 5 μ L across the entire plate after 60 minutes to quench the samples for an endpoint measurement. Fluorescent intensity was measured using excitation and emission wavelengths of 525 and 598 nm, respectively. High fluorescent intensity (DMSO with buffer) represents full inhibition of unwinding activity and low fluorescent intensity (DMSO with enzyme) represents no inhibition of unwinding activity. The potency of the compounds was determined using a four-parameter inhibition model to generate pIC₅₀, Hill slope, and maximum inhibition.

Whole-Genome Proteomics

SW48 cells were treated with DMSO or 10 μ mol/L GSK_WRN2 for 48 hours in triplicates. For harvesting, the cells were washed in PBS, pelleted, and snap-frozen in liquid N₂. Cells were lysed in 4% SDS, DNA was digested by benzonase following dilution to 1% SDS. Lysates were cleared by centrifugation, and the supernatant snap frozen until further processing. Protein digestion, labeling with tandem mass tags (TMT), pooling and prefractionation were done as described previously (55). Each of the 12 fractions was measured on

an Orbitrap Eclipse Tribrid mass spectrometer (Thermo Scientific) online-coupled to an UltiMate3000 nanoRLSC (Dionex). Peptides were separated on custom-made 50 cm × 100 μm (ID) reversed-phase columns (C18, 1.9 μm, Reprosil-Pur, Dr. Maisch) at 55°C. Gradient elution was performed from 2% acetonitrile to 40% acetonitrile in 0.1% formic acid and 3.5% DMSO within 60 minutes. MS settings were as follows: single compensation voltage FAIMS (FAIMS CV = -45), 60 k Orbitrap resolution, scan range 375 to 1,200 for the master scan. For data-dependent scans, an isolation window of 0.7, first mass at 100, HCD with a collision energy of 38%, Orbitrap resolution of 15 k with enhanced resolution mode TMT and TMTpro reagents, a maximum injection time of 60 ms, an AGC target of 100,000, and a total cycle time of 1.5 seconds was selected. Dynamic exclusion was enabled. Statistical analysis of expression proteomics was done using the statistical environment R. Proteins were filtered to have more than one quantified peptide, and annotated contaminants (based on a previously determined contaminant list) were removed. The log₂ ion intensities were quantile normalized and used as a measure for protein abundance. A linear model with an empirical Bayes variance moderation, implemented in the limma package (56), was used for differential analysis. The resulting *P* values were adjusted for multiple testing using the method of Benjamini and Hochberg. Proteins with an absolute log₂ fold change larger than log₂ (1.5) and with an adjusted *P* value below 0.05 were considered to have significantly changed under treatment. To perform GSEA, we utilized the GSEA software obtained from the Broad Institute GSEA portal (<http://software.broadinstitute.org/gsea/index.jsp>). We conducted a preranked GSEA using fold change values, applying the default parameters. To estimate the significance of enrichment, we used 1,000 gene permutations.

Cysteine Profiling

Cysteine profiling was done based on a previously published protocol (36). Jurkat cells were treated either with GSK_WRN4 at 10 or 50 μmol/L, each in triplicate or DMSO in quadruplicate for 4 hours (2 million cells per well in a 96 well plate). For harvesting, cells were washed in PBS, pelleted, and snap-frozen in liquid N₂. Cells were lysed in 4% SDS, DNA was digested by benzonase following dilution to 1% SDS. Lysates were adjusted for a protein concentration of 2.5 mg/mL. Twenty μL lysate was incubated with desthiobiotin iodoacetamide at a final concentration of 500 μmol/L for 2 hours at room temperature. Residual desthiobiotin iodoacetamide was quenched with 5 mmol/L DTT at a final concentration for 30 minutes at room temperature. Remaining free cysteines were alkylated with 20 mmol/L iodoacetamide at a final concentration for 30 minutes at room temperature in the dark. Proteins were digested, labeled with TMT and pooled as described before (55). Desthiobiotin-labeled peptides were enriched by incubation with 25 μL neutravidin beads for 1 hour at 4°C. Beads were washed three times with 2 mL 100 mmol/L HEPES and three times with 2 mL distilled H₂O. Desthiobiotin-labeled peptides were eluted by incubation with 250 μL 50% acetonitrile 0.1% TFA for 20 minutes while gently shaking. Samples were concentrated in a speedvac until dryness and prefractionated into three fractions using AssayMAP 5 μL Reversed Phase (RP-S) cartridges on a BRAVO liquid handling station according to manufacturer's instructions. Samples were measured on an Orbitrap Exploris mass spectrometer (Thermo Scientific) as described before (55). Peptide and protein identification was done as described previously except for adding the masses of 3,3'-Dithiodipropionic acid di(N-succinimidyl acrylamide) ester (DTB-IAA) on cysteine (296.184841) and on Selenocysteine (296.184841) as variable modifications (55). Analysis was done on peptide level filtered for (1% FDR) and the same quantification thresholds as described before (55). Peptides were filtered for presence of the DTB-IAA mass tag on cysteine or selenocysteine. A two-sided *t* test determined significance. Peptides with a *P* value below 0.001 and an absolute mean log₂ fold change of log₂ (1.5) were considered significantly affected.

Cell Growth Inhibition Studies (Washout Experiments)

SW48 and SW620 were cultured with 10% FBS (SAFC Sigma, #12176C-1000 mL) in RPMI medium 1640 medium (Gibco, #22400-071) and grown at 37°C and 5% CO₂ air incubator. Cells were trypsinized and counted, seeded at 500 cells per well in 100 μL culture medium in a 96-well cell culture assay plate. Compounds were diluted 1:2 from 30 μmol/L and added to 96-well plates when cells attached (24 hours post seeding). At different timepoints (1.5, 3, 5, 7, 24, 48, and 72 hours) after compound addition, culture media with compounds were aspirated. Cells were washed with 1× warm PBS gently and replaced with 100 μL fresh media. Cells were cultured for a total duration of 6 days from compound addition. Cell viability readout is performed with CellTiter-Glo One kit (Promega, #G8462) and measured on an Envision multiplate reader (PerkinElmer). Luminescence data were normalized to DMSO-treated wells, and dose-response curve fitting and plotting was performed in GraphPad Prism 7.0.

Animal Studies

All animal handling, care, and treatment procedures in this study adhered to the guidelines approved by the Institutional Animal Care and Use Committee (IACUC) and followed the Association for Assessment and Accreditation of Laboratory Animal Care standards. The *in vivo* study was performed in accordance with the GSK 3Rs (replacement, reduction, refinement) principle. Experimental protocols for SW48, SW620, and PDXs received approval from the IACUC of GSK and were conducted at the GSK US Cambridge site. LS411N and HT29 protocols received approval from the IACUC of Crown Bioscience and were carried out at the Beijing site of Crown Bioscience.

For the xenografting process, 5 × 10⁶ cells each of SW48 and SW620 were mixed in a 1:1 ratio with RPMI and Matrigel (100 μL) and then xenografted into the right flank of CrI:NU-Foxn1 nu (Strain, #088, Charles River Laboratory) female mice, aged 6 to 8 weeks and weighing 20 to 25 g. Similarly, 3 × 10⁶ cells each of LS411N and HT29 were mixed 1:1 with PBS and Matrigel or PBS alone (100 μL) and xenografted into the right flank of female BALB/c nude mice (GemPharmatech Co. Ltd), aged 6 to 7 weeks. PDX samples, sized 3 × 3 mm, were implanted using a 10G Trocar into the right hind flank of NOD. Cg-prkdcscid IL2rgtmWjl/Szj mice (Strain, #005557, The Jackson Laboratory), aged 6 to 8 weeks and weighing more than 17 g.

Once the tumors reached approximately 80 to 140 mm³, animals were randomly assigned into groups based on individual tumor size using a stratified for SW48, SW620, and PDX and matched distribution for LS411N and HT29 randomization method. Body weight and tumor volume were measured 2 times per week using an electric caliper (Fowler Ultra-Cal V) and an Ohaus electronic scale (STX421), with data automatically recorded in the Study Log. Tumor volume was calculated using the formula $0.5 \times L \times W^2$, in which *L* is the tumor length (the longest dimension) and *W* is the tumor width (perpendicular to *L*). Tumor growth inhibition was calculated using the equation $\text{Mean \% } \Delta \text{ Inhibition} = \frac{[(\text{mean}(C) - \text{mean}(CO)) - (\text{mean}(T) - \text{mean}(TO))]}{[\text{mean}(C) - \text{mean}(CO)]} \times 100\%$.

For pharmacodynamic analysis of GSK_WRN4, tumors were collected at different time point 24 hours after the final dose. Tumor tissues were divided into two portions: one for snap freezing and the other fixed in 10% formalin for 24 hours and then embedded in paraffin for histologic analysis. GSK_WRN4 was freshly prepared using 20% propylene glycol, and animals received daily oral administration of GSK_WRN4 at a selected dose with a volume of 10 mL/kg. Statistical analyses were performed using two-way ANOVA to compare control vs. GSK_WRN4 treatment at different time points and relative body weight (as a percentage of day 0, between control and GSK_WRN4 at different time points) using Prism GraphPad Prism 9 (GraphPad Software, Inc.). All data are presented as mean ± standard error. Statistical significance was determined by main effects found via Tukey *post hoc* test, with a *P* value of less than 0.05 considered

statistically significant. For pharmacokinetic studies, GSK_WRN4 was orally administered in the male BALB/c mouse as a suspension formulation. Two mice were used for the pharmacokinetic study under fed conditions. The compound was formulated in 1% aqueous methyl cellulose, in a white fluid suspension and administered through oral gavage. The blood of mice was sampled via tail snip method at 0, 0.25, 0.5, 1.5, 2, 4, and 8 hours after dosing. Twenty-five μ L blood from each sample was used for LC/MS-MS analysis of blood concentrations of GSK_WRN4.

In Vivo Tumor Histologic Staining

All histologic analyses were performed by HistoWiz, Inc. Standard procedures for hematoxylin and eosin staining, Masson's trichrome staining, and IHC were utilized to assess morphology, fibrosis/extracellular matrix composition, and specific protein expression within the tissue samples, respectively. For the IHC, the following primary antibodies were employed: Ki67 (ab15580, 1:800, Abcam), phospho-Histone H2A.X (γ H2AX; CST9718, 1:800, Cell Signaling Technology), phospho-KAP1 (S824; ab2438570, 1:1,000, Abcam), p21 (ab109520, 1:100, Abcam), and cleaved caspase 3 (CST9661, 1:300, Cell Signaling Technology).

Validation Experiments in the Independent Cohort of Colorectal Cancer Organoids

The organoid screening derived from patient with colon cancer was performed by CrownBio Science. A thorough examination was conducted using a comprehensive panel consisting exclusively of GSK_WRN4, which was applied to the organoids. To evaluate the effects of the treatment, a 5-day CellTiter-Glo Luminescent Cell Viability Assay was employed, which assessed the viability changes occurring in the organoids in response to the GSK_WRN4. Deficiencies in the MMR system were evaluated using an MMR panel test through IHC. This test specifically assessed the expression of MLH1, MSH2, MSH6, and PMS2. The analysis was conducted at NeoGenomics Laboratories.

Data Analysis

Heatmaps in the biomarker analysis section were created using the `geom_tile` function from the `ggplot2` package in R. The plots and graphs were generated using GraphPad and Spotfire software. The WRN dependency for cell lines was determined from an integrated dataset of essentiality data, curated from multiple sources including Project Score (<https://score.depmap.sanger.ac.uk/>) and the Dependency Map (DepMap; <https://depmap.org/portal/>), as recently described (57). The analysis in Fig. 3C, including the calculation of Pearson correlation, *P* values, and Benjamini-Hochberg adjusted *q*-values, was conducted using Python NumPy and statistics libraries.

Data Availability

The data generated in this study are available within the article and its supplementary data files. TrAEL-seq sequencing data have been deposited in the Gene Expression Omnibus repository under the accession number GSE253197. Base editing sequencing data have been deposited in the EGA database under accession number EGAD00001015355.

Authors' Disclosures

M.J. Garnett reports research grants from AstraZeneca, GlaxoSmithKline, and Astex Pharmaceuticals, as well as being a founder and advisor at Mosaic Therapeutics. E.E. Voest is a founder and advisor at Mosaic Therapeutics. G. Picco serves in a consultant role for Mosaic Therapeutics. All authors listed with an affiliation to GlaxoSmithKline (GSK) are GSK employees except J.E. Cottom and

Y. Peng, who are no longer GSK employees. S.F. Vieira is currently employed at AstraZeneca. No disclosures were reported by the other authors.

Authors' Contributions

G. Picco: Conceptualization, resources, data curation, formal analysis, supervision, funding acquisition, validation, investigation, visualization, methodology, writing—original draft, project administration, writing—review and editing. **Y. Rao:** Conceptualization, data curation, formal analysis, supervision, validation, investigation, visualization, writing—original draft. **A. Al Saedi:** Validation, investigation. **Y. Lee:** Formal analysis, validation, investigation, visualization. **S.F. Vieira:** Conceptualization, data curation, formal analysis, supervision, funding acquisition, validation, investigation, visualization, methodology, writing—original draft, project administration, writing—review and editing. **S. Bhosle:** Data curation, formal analysis. **K. May:** Investigation. **C. Herranz-Ors:** Formal analysis, visualization. **S.J. Walker:** Validation. **R. Shenje:** Investigation. **C. Dincer:** Formal analysis, investigation, visualization. **F. Gibson:** Resources, investigation. **R. Banerjee:** Formal analysis, validation, investigation. **Z. Hewitson:** Resources, validation, investigation. **T. Werner:** Resources, data curation, validation, investigation. **J.E. Cottom:** Formal analysis, supervision, investigation, project administration. **Y. Peng:** Resources, formal analysis, validation, investigation. **N. Deng:** Conceptualization, resources, data curation, supervision, funding acquisition, validation, investigation, writing—original draft. **P. Landis:** Resources, data curation, formal analysis, supervision, validation, investigation, project administration. **D. Conticelli:** Conceptualization, resources, data curation, formal analysis, supervision, funding acquisition, validation, investigation, writing—original draft, project administration. **K. McCarten:** Conceptualization, resources, data curation, formal analysis, supervision, funding acquisition, validation, investigation, writing—original draft, project administration. **J. Bush:** Resources, data curation, formal analysis, supervision, validation, investigation, project administration. **M. Sharma:** Conceptualization, resources, data curation, formal analysis, supervision, funding acquisition, validation, investigation, writing—original draft, project administration. **H. Lightfoot:** Conceptualization, resources, data curation, formal analysis, supervision, funding acquisition, validation, investigation, visualization, writing—original draft, project administration. **D. House:** Conceptualization, resources, data curation, formal analysis, supervision, funding acquisition, investigation, visualization, writing—original draft, project administration. **E. Milford:** Investigation. **E.K. Grant:** Investigation. **M.P. Glogowski:** Investigation. **C.D. Wagner:** Investigation. **M. Bantscheff:** Investigation. **A. Rutkowska-Klute:** Data curation, formal analysis, supervision, validation, investigation, visualization. **C. Network UK Group:** Resources. **F. Zappacosta:** Conceptualization, resources, data curation, formal analysis, supervision, funding acquisition, validation, investigation, visualization, writing—original draft, project administration. **J. Pettinger:** Conceptualization, resources, data curation, formal analysis, supervision, funding acquisition, validation, investigation, visualization, writing—original draft, project administration. **S. Barthorpe:** Conceptualization, resources, data curation, formal analysis, supervision, funding acquisition, validation, investigation, visualization, writing—original draft, project administration. **C. Eberl:** Conceptualization, resources, data curation, formal analysis, supervision, funding acquisition, validation, investigation, visualization, writing—original draft, project administration. **B.T. Jones:** Conceptualization, resources, formal analysis, supervision, funding acquisition, validation, investigation, visualization, writing—original draft, project administration. **J.L. Schneck:** Conceptualization, resources, data curation, formal analysis, supervision, funding acquisition, validation, investigation, visualization, writing—original draft, project administration. **D.J. Murphy:** Conceptualization, resources,

data curation, formal analysis, supervision, funding acquisition, validation, investigation, visualization, writing—original draft, project administration. **E.E. Voest:** Conceptualization, resources, formal analysis, supervision, funding acquisition, validation, investigation, visualization, writing—original draft, project administration. **J.P. Taygerly:** Supervision, investigation. **M.P. DeMartino:** Resources, validation, investigation, visualization. **M.A. Coelho:** Resources, data curation, formal analysis, supervision, validation, investigation, visualization. **J. Houseley:** Conceptualization, resources, data curation, formal analysis, supervision, funding acquisition, validation, investigation, visualization, writing—original draft, project administration. **G. Sharma:** Conceptualization, resources, supervision, validation, investigation, visualization, writing—original draft, project administration. **B. Schwartz:** Conceptualization, resources, supervision, funding acquisition, validation, investigation, writing—original draft, project administration. **M.J. Garnett:** Conceptualization, resources, supervision, validation, investigation, visualization, writing—original draft, project administration. Experiments were conducted by GP, AAS, SV, SW, RB, DC, EM, EKG, CW, JP, RS, BJ, MG, DM, YL, ND, JC, YZ, LN, EN and YP.

Acknowledgments

We thank the Garnett laboratory, Cellular Generation and Phenotyping facility, gene editing team, and drug screening teams at the Sanger Institute for data generation and assistance. We thank Emre Karakoc for informatic support and Inigo Barrio Hernandez for help with protein rendering. We thank Christian Frey, Diana Munoz, and Anjana Srivatsan for providing feedback on the manuscript and for helpful discussion of the results. This research was funded in whole, or in part, by Wellcome Trust Grant 206194. For open access, the author has applied a CC BY public copyright license to any author accepted manuscript version arising from this submission. TrAEL-seq library sequencing and processing were performed by Genomics—Geno06 and Bioinformatics—Bioinf01 at the Babraham Institute, which receive financial support from the Institute Core Capability Grant (BBSRC CCG). Funding: J. Houseley—BBSRC (BI Epigenetics ISP; BBS/E/B/000C0523); K. May—BBSRC (BB/W509917/1).

Note

Supplementary data for this article are available at Cancer Discovery Online (<http://cancerdiscovery.aacrjournals.org/>).

Received January 20, 2024; revised March 26, 2024; accepted April 5, 2024; published first April 6, 2024.

REFERENCES

- Cortes-Ciriano I, Lee S, Park W-Y, Kim T-M, Park PJ. A molecular portrait of microsatellite instability across multiple cancers. *Nat Commun* 2017;8:15180.
- Bonneville R, Krook MA, Kautto EA, Miya J, Wing MR, Chen H-Z, et al. Landscape of microsatellite instability across 39 cancer types. *JCO Precis Oncol* 2017;2017:PO.17.00073.
- Toh J, Spring K. 582P—Microsatellite Instability (MSI) status and prognosis in colorectal cancer: meta-analysis. *Ann Oncol* 2019;30:v220.
- Zhu L, Li Z, Wang Y, Zhang C, Liu Y, Qu X. Microsatellite instability and survival in gastric cancer: a systematic review and meta-analysis. *Mol Clin Oncol* 2015;3:699–705.
- Cohen R, Rousseau B, Vidal J, Colle R, Diaz LA Jr, André T. Immune checkpoint inhibition in colorectal cancer: microsatellite instability and beyond. *Target Oncol* 2020;15:11–24.
- de Vries NL, van de Haar J, Veninga V, Chalabi M, Ijsselsteijn ME, van der Ploeg M, et al. $\gamma\delta$ T cells are effectors of immunotherapy in cancers with HLA class I defects. *Nature* 2023;613:743–50.
- Chalabi M, Fanchi LF, Dijkstra KK, Van den Berg JG, Aalbers AG, Sikorska K, et al. Neoadjuvant immunotherapy leads to pathological responses in MMR-proficient and MMR-deficient early-stage colon cancers. *Nat Med* 2020;26:566–76.
- Overman MJ, Lonardi S, Wong KYM, Lenz H-J, Gelsomino F, Aglietta M, et al. Durable clinical benefit with nivolumab plus ipilimumab in DNA mismatch repair-deficient/microsatellite instability-high metastatic colorectal cancer. *J Clin Oncol* 2018;36:773–9.
- André T, Tougeron D, Piessen G, de la Fouchardière C, Louvet C, Adenis A, et al. Neoadjuvant nivolumab plus ipilimumab and adjuvant nivolumab in localized deficient mismatch repair/microsatellite instability-high gastric or esophagogastric junction adenocarcinoma: the GERCOR NEONIPIGA phase II study. *J Clin Oncol* 2023;41:255–65.
- Kwon M, An M, Klempner SJ, Lee H, Kim K-M, Sa JK, et al. Determinants of response and intrinsic resistance to PD-1 blockade in microsatellite instability-high gastric cancer. *Cancer Discov* 2021;11:2168–85.
- Bhamidipati D, Subbiah V. Tumor-agnostic drug development in dMMR/MSI-H solid tumors. *Trends Cancer* 2023;9:828–39.
- Chow RD, Michaels T, Bellone S, Hartwich TMP, Bonazzoli E, Iwasaki A, et al. Distinct mechanisms of mismatch-repair deficiency delineate two modes of response to anti-PD-1 immunotherapy in endometrial carcinoma. *Cancer Discov* 2023;13:312–31.
- Brosh RM Jr. DNA helicases involved in DNA repair and their roles in cancer. *Nat Rev Cancer* 2013;13:542–58.
- Chu WK, Hickson ID. RecQ helicases: multifunctional genome caretakers. *Nat Rev Cancer* 2009;9:644–54.
- Behan FM, Iorio F, Picco G, Gonçalves E, Beaver CM, Migliardi G, et al. Prioritization of cancer therapeutic targets using CRISPR-Cas9 screens. *Nature* 2019;568:511–6.
- Chan EM, Shibue T, McFarland JM, Gaeta B, Ghandi M, Dumont N, et al. WRN helicase is a synthetic lethal target in microsatellite unstable cancers. *Nature* 2019;568:551–6.
- Lieb S, Blaha-Ostermann S, Kamper E, Rippka J, Schwarz C, Ehrenhöfer-Wölfer K, et al. Werner syndrome helicase is a selective vulnerability of microsatellite instability-high tumor cells. *Elife* 2019;8:e43333.
- Aggarwal M, Sommers JA, Shoemaker RH, Brosh RM Jr. Inhibition of helicase activity by a small molecule impairs Werner syndrome helicase (WRN) function in the cellular response to DNA damage or replication stress. *Proc Natl Acad Sci U S A* 2011;108:1525–30.
- van Wietmarschen N, Sridharan S, Nathan WJ, Tubbs A, Chan EM, Callen E, et al. Repeat expansions confer WRN dependence in microsatellite-unstable cancers. *Nature* 2020;586:292–8.
- Picco G, Cattaneo CM, van Vliet EJ, Crisafulli G, Rospo G, Consonni S, et al. Werner helicase is a synthetic-lethal vulnerability in mismatch repair-deficient colorectal cancer refractory to targeted therapies, chemotherapy, and immunotherapy. *Cancer Discov* 2021;11:1923–37.
- Aggarwal M, Banerjee T, Sommers JA, Brosh RM Jr. Targeting an Achilles' heel of cancer with a WRN helicase inhibitor. *Cell Cycle* 2013;12:3329–35.
- Morales-Juarez DA, Jackson SP. Clinical prospects of WRN inhibition as a treatment for MSI tumours. *NPJ Precis Oncol* 2022;6:85.
- Moles R, Bai XT, Chaib-Mezrag H, Nicot C. WRN-targeted therapy using inhibitors NSC 19630 and NSC 617145 induce apoptosis in HTLV-1-transformed adult T-cell leukemia cells. *J Hematol Oncol* 2016;9:121.
- Parker MJ, Lee H, Yao S, Irwin S, Hwang S, Belanger K, et al. Identification of 2-sulfonyl/sulfonamide pyrimidines as covalent inhibitors of WRN using a multiplexed high-throughput screening assay. *Biochemistry* 2023;62:2147–60.
- Rao Y, Srivatsan A, Liimatta M, Munoz D, Quirrit J, Shi J, et al. Abstract 1628: a small-molecule inhibitor of WRN selectively kills MSI-H cancer cells and phenocopies WRN genetic defects. *Cancer Res* 2023;83(Suppl 7):1628.
- Cortes-Cros M, Moebitz H, Barbe S, Blank J, Bordas V, Clementi G, et al. Abstract PR007: discovery of HRO761, a novel, first-in-class clinical stage WRN inhibitor with potent and selective anti-tumor activity in cancers with microsatellite instability. *Mol Cancer Ther* 2023;22(Suppl 12):PR007.

27. Mullard A. What's next for the synthetic lethality drug discovery engine? *Nat Rev Drug Discov* 2022;21:477–9.
28. Gaudelli NM, Komor AC, Rees HA, Packer MS, Badran AH, Bryson DI, et al. Programmable base editing of A•T to G•C in genomic DNA without DNA cleavage. *Nature* 2017;551:464–71.
29. Komor AC, Kim YB, Packer MS, Zuris JA, Liu DR. Programmable editing of a target base in genomic DNA without double-stranded DNA cleavage. *Nature* 2016;533:420–4.
30. Cheng J, Novati G, Pan J, Bycroft C, Žemgulytė A, Applebaum T, et al. Accurate proteome-wide missense variant effect prediction with AlphaMissense. *Science* 2023;381:eadg7492.
31. Coelho MA, Cooper S, Strauss ME, Karakoc E, Bhosle S, Gonçalves E, et al. Base editing screens map mutations affecting interferon- γ signaling in cancer. *Cancer Cell* 2023;41:288–303.e6.
32. Dwane L, Behan FM, Gonçalves E, Lightfoot H, Yang W, van der Meer D, et al. Project score database: a resource for investigating cancer cell dependencies and prioritizing therapeutic targets. *Nucleic Acids Res* 2021;49:D1365–72.
33. Newman JA, Gavard AE, Lieb S, Ravichandran MC, Hauer K, Werni P, et al. Structure of the helicase core of Werner helicase, a key target in microsatellite instability cancers. *Life Sci Alliance* 2021;4:e202000795.
34. Johansson H, Isabella Tsai Y-C, Fantom K, Chung C-W, Kümper S, Martino L, et al. Fragment-based covalent ligand screening enables rapid discovery of inhibitors for the RBR E3 ubiquitin ligase HOIP. *J Am Chem Soc* 2019;141:2703–12.
35. Sommers JA, Kulikowicz T, Croteau DL, Dexheimer T, Dorjsuren D, Jadhav A, et al. A high-throughput screen to identify novel small molecule inhibitors of the Werner syndrome helicase-nuclease (WRN). *PLoS One* 2019;14:e02110525.
36. Kuljanin M, Mitchell DC, Schweppe DK, Gikandi AS, Nusinow DP, Bulloch NJ, et al. Reimagining high-throughput profiling of reactive cysteines for cell-based screening of large electrophile libraries. *Nat Biotechnol* 2021;39:630–41.
37. Kategaya L, Perumal SK, Hager JH, Belmont LD. Werner syndrome helicase is required for the survival of cancer cells with microsatellite instability. *iScience* 2019;13:488–97.
38. Hao S, Tong J, Jha A, Risnik D, Lizardo D, Lu X, et al. Synthetical lethality of Werner helicase and mismatch repair deficiency is mediated by p53 and PUMA in colon cancer. *Proc Natl Acad Sci U S A* 2022; 119:e2211775119.
39. Kara N, Krueger F, Rugg-Gunn P, Houseley J. Genome-wide analysis of DNA replication and DNA double-strand breaks using TrAEL-seq. *Plos Biol* 2021;19:e3000886.
40. Ryan CJ, Devakumar LPS, Pettitt SJ, Lord CJ. Complex synthetic lethality in cancer. *Nat Genet* 2023;55:2039–48.
41. Brown JS, O'Carrigan B, Jackson SP, Yap TA. Targeting DNA repair in cancer: beyond PARP inhibitors. *Cancer Discov* 2017;7:20–37.
42. Farmer H, McCabe N, Lord CJ, Tutt ANJ, Johnson DA, Richardson TB, et al. Targeting the DNA repair defect in BRCA mutant cells as a therapeutic strategy. *Nature* 2005;434:917–21.
43. Zong D, Koussa NC, Cornwell JA, Pankajam AV, Kruhlak MJ, Wong N, et al. Comprehensive mapping of cell fates in microsatellite unstable cancer cells supports dual targeting of WRN and ATR. *Genes Dev* 2023;37:913–28.
44. Boehm JS, Garnett MJ, Adams DJ, Francies HE, Golub TR, Hahn WC, et al. Cancer research needs a better map. *Nature* 2021;589:514–6.
45. van der Meer D, Barthorpe S, Yang W, Lightfoot H, Hall C, Gilbert J, et al. Cell model passports—a hub for clinical, genetic and functional datasets of preclinical cancer models. *Nucleic Acids Res* 2019;47:D923–9.
46. Jaaks P, Coker EA, Vis DJ, Edwards O, Carpenter EF, Leto SM, et al. Effective drug combinations in breast, colon and pancreatic cancer cells. *Nature* 2022;603:166–73.
47. Vis DJ, Bombardelli L, Lightfoot H, Iorio F, Garnett MJ, Wessels LF. Multilevel models improve precision and speed of IC₅₀ estimates. *Pharmacogenomics* 2016;17:691–700.
48. Price S, Bhosle S, Gonçalves E, Li X, McClurg DP, Barthorpe S, et al. A suspension technique for efficient large-scale cancer organoid culturing and perturbation screens. *Sci Rep* 2022;12:5571.
49. Gonçalves E, Thomas M, Behan FM, Picco G, Pacini C, Allen F, et al. Minimal genome-wide human CRISPR-Cas9 library. *Genome Biol* 2021;22:40.
50. Coelho MA, Li S, Pane LS, Firth M, Ciotta G, Wrigley JD, et al. BE-FLARE: a fluorescent reporter of base editing activity reveals editing characteristics of APOBEC3A and APOBEC3B. *BMC Biol* 2018;16:150.
51. Kluesner MG, Lahr WS, Lonetree C-L, Smeester BA, Qiu X, Slipek NJ, et al. CRISPR-Cas9 cytidine and adenosine base editing of splice-sites mediates highly-efficient disruption of proteins in primary and immortalized cells. *Nat Commun* 2021;12:2437.
52. Friedrich K, Lee L, Leistritz DF, Nürnberg G, Saha B, Hisama FM, et al. WRN mutations in Werner syndrome patients: genomic rearrangements, unusual intronic mutations and ethnic-specific alterations. *Hum Genet* 2010;128:103–11.
53. Picco G, Chen ED, Alonso LG, Behan FM, Gonçalves E, Bignell G, et al. Functional linkage of gene fusions to cancer cell fitness assessed by pharmacological and CRISPR-Cas9 screening. *Nat Commun* 2019; 10:2198.
54. Adams A, Burgess JL, Bury MJ, Demartino MP, Dowdell SE, Glogowski MP, et al. inventor; Cyclic vinyl sulfone compounds as wrn inhibitors. World Intellectual Property Organization (WIPO), World Patent WO2023062575 A1 2023 Apr 20.
55. Zinn N, Werner T, Doce C, Mathieson T, Boecker C, Sweetman G, et al. Improved proteomics-based drug mechanism-of-action studies using 16-plex isobaric mass tags. *J Proteome Res* 2021;20:1792–801.
56. Ritchie ME, Phipson B, Wu D, Hu Y, Law CW, Shi W, et al. Limma powers differential expression analyses for RNA-sequencing and microarray studies. *Nucleic Acids Res* 2015;43:e47.
57. Pacini C, Duncan E, Gonçalves E, Gilbert J, Bhosle S, Horswell S, et al. A comprehensive clinically informed map of dependencies in cancer cells and framework for target prioritization. *Cancer Cell* 2024;42: 301–16.e9.